Operational Analyses and Control Scheme of Nine-Arm Modular Multilevel Converter

Futian Qin, *Student Member, IEEE*, Feng Gao, *Senior Member, IEEE*,
and Chenghui Zhang, *Senior Member, IEEE*

***Abstract*—Nine-arm modular multilevel converter (9A-MMC) can be applied in many medium-/high-voltage applications with two sets of three-phase terminals, such as medium-voltage dual-motor drives and unified power flow controller, to replace two conventional modular multilevel converters for reducing the volume and cost. This article thoroughly investigated the operational principle of 9A-MMC, and proposed a unique operational mode that the number of submodules in each arm can be a variable. The mathematical model of 9A-MMC and steady-state analyses of capacitor voltage fluctuations and circulating current were studied in this article as well. Subsequently, a complete control scheme of 9A-MMC, including capacitor voltage balancing control and circulating current suppression control is systematically presented. Finally, the simulation and experimental results verified the performance of 9A-MMC and the effectiveness of the presented control methods.**

***Index Terms*—Capacitor voltage fluctuations, circulating current, nine-arm modular multilevel converter (9A-MMC), variable submodule (SM) number.**

I. Introduction

MODULAR multilevel converter (MMC) has become the most attractive multilevel topology in medium-/high-voltage applications, such as high-voltage direct current transmission systems [1]–[3], flexible ac transmission systems [4]–[6], medium-voltage motor drives [7], [8], etc., since it was first proposed in [9] and [10], due to its prominent advantages of modularity, scalability, and superior harmonic performance.

In medium-/high-voltage applications, there are some applications including two sets of three-phase terminals, such as medium-voltage dual-motor drives, unified power flow controller, where two conventional MMCs are usually employed [6], [11]. Fortunately, it is possible to integrate two MMCs into one compact nine-arm MMC (9A-MMC) with dual ports to minimize the system footprint and cost [12]–[15], being similar to the integration principle of nine-switch converter [16], [17].

9A-MMC was first proposed in [12], where the dc side of submodules (SMs) was replaced by dc sources to simplify the control scheme design. So, the circulating current suppression control (CCSC) and capacitor voltage balancing control (CVBC), which are two critical issues in MMC, were not considered in [12]. In [13]–[15], 9A-MMC was applied to power medium-voltage six-phase induction motors. The control scheme of 9A-MMC in [13] and [15] is a simple open-loop control, and only CVBC realized by sorting methods was included, while the CCSC for 9A-MMC was not investigated. Although circulating current suppression was considered in [14], the method of attenuating circulating current is realized by adding extra hardware devices (two parallel resonant filters for each leg) and only second-order harmonics of circulating current was suppressed. It is obvious that this method is at the expense of increased component counts and system losses. Moreover, only the operation state that the amplitude of two output terminals is equal and phase shift between two terminals is fixed at 30° or 60° was taken into account in [13]–[15]. And the number of SMs in each arm of 9A-MMC presented in [12]–[15] is equal and invariable, which is identical to the design of conventional MMC, where the upper and lower arms are symmetrical [18].

However, the upper, middle, and lower arms of 9A-MMC do not have to be symmetrical in implementation, because the amplitudes and relative phase angle of upper and lower output terminals in 9A-MMC can be different. Such unique operational principle has so far not been reported and investigated. So, this article first fully studies the operational principle and mathematical model of 9A-MMC and then proposes a complete control scheme for 9A-MMC. Simulation and experimental results verified the theoretical findings.

II. Topology and Mathematical Model of 9A-MMC

A. Topology of 9A-MMC

As illustrated in Fig. 1, the conventional solution for the medium-/high-voltage applications with two sets of three-phase terminals is to assume two three-phase MMCs, which are composed of six legs, where each leg consists of two arms and each arm comprises N series-connected half-bridge SMs and a series inductor L_{arm}. The SMs in each arm can be individually and selectively controlled to generate the desired sinusoidal voltage

---

Manuscript received January 14, 2019; revised June 6, 2019; accepted August 6, 2019. Date of publication August 12, 2019; date of current version January 10, 2020. This work was supported in part by the National Natural Science Foundation of China under Grant 51722704, in part by the Shandong Provincial Natural Science Foundation, China, under Grant JQ201717, in part by the Foundation for Innovative Research Groups of National Natural Science Foundation of China under Grant 61821004, and in part by The Key Project of National Natural Science Foundation of China under Grant 61733010. Recommended for publication by Associate Editor H. Wang. *(Corresponding author: Feng Gao.)*

F. Qin and F. Gao are with the Key Lab of Power System Intelligent Dispatch and Control, Ministry of Education, Shandong University, Jinan 250061, China (e-mail: ft_qin@163.com; fgao@sdu.edu.cn).

C. Zhang is with the School of Control Science and Engineering, Shandong University, Jinan 250061, China (e-mail: zchui@sdu.edu.cn).

Color versions of one or more of the figures in this article are available online at http://ieeexplore.ieee.org.

Digital Object Identifier 10.1109/TPEL.2019.2935032

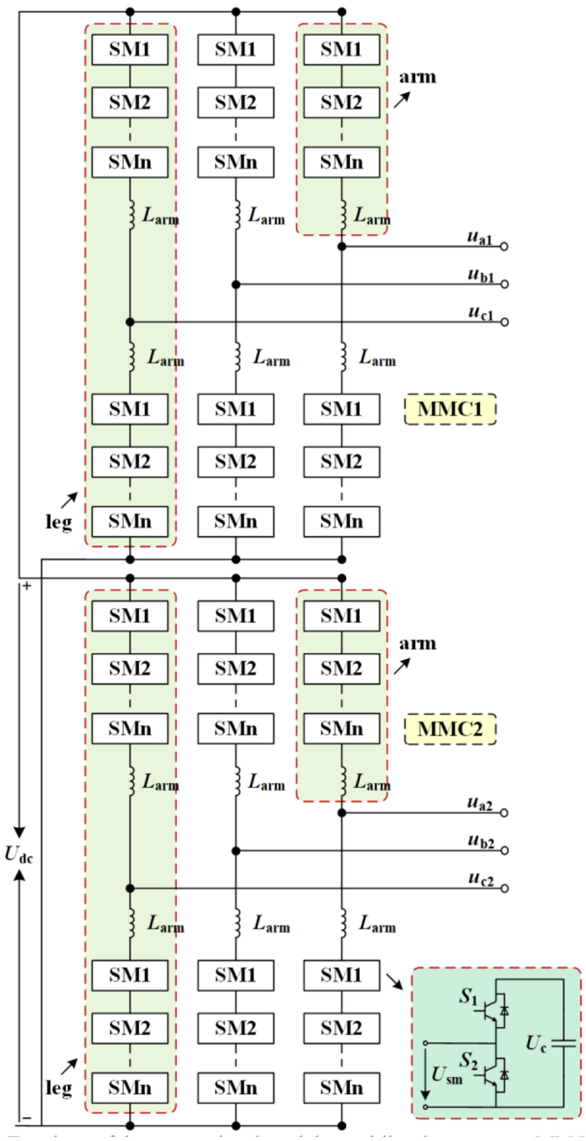

Fig. 1. Topology of the conventional modular multilevel converters (MMC) for powering two loads.

and the arm inductor can suppress the fault current rising rate and the high-frequency components in arm current [19].

Comparatively, 9A-MMC can be deemed as a combination of two conventional MMCs with double function middle arms, and it is topologically similar to the nine-switch converter. As shown in Fig. 2, 9A-MMC consists of three legs, and each leg is formed by three arms, where k_1, k_2, and k_3 represent the number of SMs in upper, middle, and lower arms, respectively, L_u and L_l are arm inductors in upper and lower arm with $L_u = L_l$, and the half-bridge SM is also employed. Being different, the number of SMs in upper, middle, and lower arms can be unequal, and only upper and lower arms equip with arm inductors.

B. Mathematical Model of 9A-MMC

The simplified equivalent model of three-phase 9A-MMC is shown in Fig. 3, where the SMs are considered as the controlled voltage sources and the voltage of each arm is the combination of these controlled voltage sources. According to the equivalent model, the mathematical expression of upper, middle, and lower arms' voltages and currents in j (j = a, b, or c) phase can be

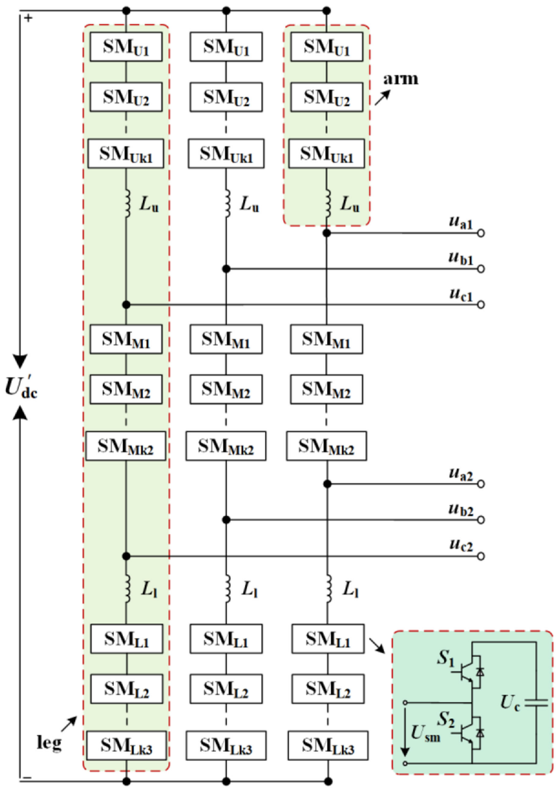

Fig. 2. Topology of nine-arm modular multilevel converter (9A-MMC).

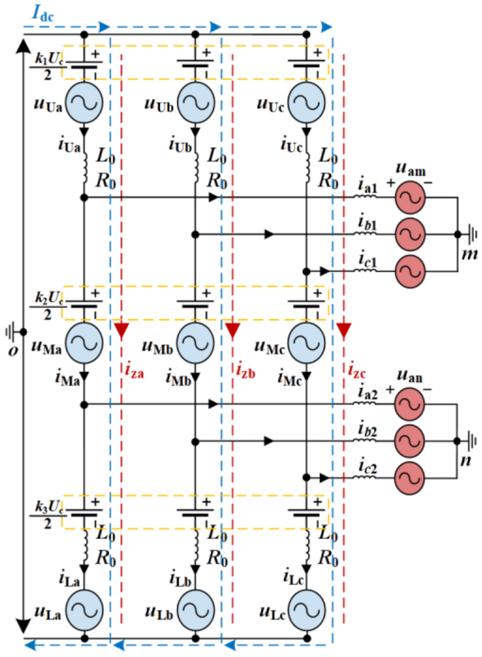

Fig. 3. Equivalent model of 9A-MMC.

obtained as follows:

$$u_{Uj} = \frac{1}{2}k_1 U_c - u_{jm} \quad (1)$$

$$u_{Mj} = \frac{1}{2}k_2 U_c + u_{jm} - u_{jn} \quad (2)$$

$$u_{Lj} = \frac{1}{2}k_3 U_c + u_{jn} \quad (3)$$

$$i_{Uj} = i_{zj} + \frac{1}{2}(i_{j1} + i_{j2}) \quad (4)$$

$$i_{Mj} = i_{zj} - \frac{1}{2}(i_{j1} - i_{j2}) \quad (5)$$

$$i_{Lj} = i_{zj} - \frac{1}{2}(i_{j1} + i_{j2}) \quad (6)$$

where u_{Uj}, u_{Mj}, and u_{Lj} are the upper, middle, and lower arm voltages of *j* phase, while i_{Uj}, i_{Mj}, and i_{Lj} are the upper, middle, and lower arm currents of *j* phase, U_c is the rated SM capacitor voltage, k_1, k_2, and k_3 are the number of SMs in upper, middle, and lower arms, u_{jm}, u_{jn}, i_{j1}, and i_{j2} are the upper and lower output voltages and currents of *j* phase, i_{zj} is the circulating current of *j* phase. Based on (1)–(3), the relationships between arm voltages and output voltages can be derived as follows:

$$u_{jm} = \frac{u_{Mj} + u_{Lj} - u_{Uj}}{2} - \frac{k_2 + k_3 - k_1}{4}U_c \quad (7)$$

$$u_{jn} = \frac{u_{Lj} - u_{Mj} - u_{Uj}}{2} - \frac{k_3 - k_2 - k_1}{4}U_c. \quad (8)$$

The dc-side voltage can be derived as follows:

$$U_{\mathrm{dc}} = \frac{k_1 + k_2 + k_3}{2}U_c. \quad (9)$$

According to (4) and (6), the circulating current of *j* phase can be expressed as follows:

$$i_{zj} = \frac{(i_{Uj} + i_{Lj})}{2}. \quad (10)$$

C. Steady-State Analyses of Capacitor Voltage Fluctuations and Circulating Current

Taking phase A as an example, the upper and lower output phase voltages and currents of 9A-MMC can be assumed to be as follows:

$$u_{\mathrm{am}}(t) = u_{a1}\sin(\omega t) \quad (11)$$

$$u_{\mathrm{an}}(t) = u_{a2}\sin(\omega t + \theta) \quad (12)$$

$$i_{a1}(t) = i_{a1}\sin(\omega t - \varphi_1) \quad (13)$$

$$i_{a2}(t) = i_{a2}\sin(\omega t + \theta - \varphi_2) \quad (14)$$

where u_{a1} and u_{a2} are the amplitude of upper and lower output phase voltages, while i_{a1} and i_{a2} are the amplitude of upper and lower output currents, θ is the phase shift between two output voltages, φ_1 and φ_2 are the power factor angle of upper and lower output terminals.

Ideally, i_{zj} only consists of dc component, and its ac components should be effectively mitigated by CCSC. Then, substituting i_{a1} and i_{a2} in (4)–(6) by (13) and (14), the upper, middle, and lower arm currents of phase A can be rewritten as follows:

$$i_{Ua}(t) = \frac{1}{3}I_{\mathrm{dc}} + \frac{1}{2}[i_{a1}\sin(\omega t - \varphi_1) + i_{a2}\sin(\omega t + \theta - \varphi_2)] \quad (15)$$

$$i_{Ma}(t) = \frac{1}{3}I_{\mathrm{dc}} - \frac{1}{2}[i_{a1}\sin(\omega t - \varphi_1) - i_{a2}\sin(\omega t + \theta - \varphi_2)] \quad (16)$$

$$i_{La}(t) = \frac{1}{3}I_{\mathrm{dc}} - \frac{1}{2}[i_{a1}\sin(\omega t - \varphi_1) + i_{a2}\sin(\omega t + \theta - \varphi_2)] \quad (17)$$

where I_{dc} is the dc-side current. According to (1)–(3), (11) and (12), and neglecting the high-frequency components of switching function, the switching functions of upper, middle, and lower arms can be defined as follows:

$$f_{Ua}(t) = \frac{1}{2}[1 - M_1\sin(\omega t)] \quad (18)$$

$$f_{Ma}(t) = \frac{1}{2}\left[1 + \frac{k_1}{k_2}M_1\sin(\omega t) - \frac{k_3}{k_2}M_2\sin(\omega t + \theta)\right] \quad (19)$$

$$f_{La}(t) = \frac{1}{2}[1 + M_2\sin(\omega t + \theta)] \quad (20)$$

where $M_1 = \frac{2u_{a1}}{k_1 U_c}$ and $M_2 = \frac{2u_{a2}}{k_3 U_c}$ refer to the modulation ratios of upper and lower output terminals.

The arm current will be coupled to the dc side of SMs by switching actions. Then, the average capacitor currents in upper, middle, and lower arms can be determined as follows:

$$i_{c\_Ua}(t) = f_{Ua}(t)i_{Ua}(t) = i_{c\_Ua\_\mathrm{dc}} + i_{c\_Ua\_1\omega} + i_{c\_Ua\_2\omega} \quad (21)$$

$$i_{c\_Ma}(t) = f_{Ma}(t)i_{Ma}(t) = i_{c\_Ma\_\mathrm{dc}} + i_{c\_Ma\_1\omega} + i_{c\_Ma\_2\omega} \quad (22)$$

$$i_{c\_La}(t) = f_{La}(t)i_{La}(t) = i_{c\_La\_\mathrm{dc}} + i_{c\_La\_1\omega} + i_{c\_La\_2\omega} \quad (23)$$

where $i_{c\_Ua\_\mathrm{dc}}$, $i_{c\_Ua\_1\omega}$, $i_{c\_Ua\_2\omega}$, $i_{c\_Ma\_\mathrm{dc}}$, $i_{c\_Ma\_1\omega}$, $i_{c\_Ma\_2\omega}$, $i_{c\_La\_\mathrm{dc}}$, $i_{c\_La\_1\omega}$, and $i_{c\_La\_2\omega}$ are dc and ac components of capacitor currents in upper, middle, and lower arms, respectively. Their detailed expressions are demonstrated in Appendix A.

The capacitor will be continuously charged or discharged by the dc component of the capacitor current. Therefore, the dc components of the capacitor current shown in (A1), (A4), and (A7) should be equal to 0 during the steady-state operation, otherwise the capacitor voltage will increase or decrease continuously. This also indicates that the transferred active power between the dc-side and ac-side should be equal under steady state. The dc-side current can then be expressed as follows:

$$I_{\mathrm{dc}} = \frac{(k_1 + k_2)i_{a1}M_1\cos(\varphi_1) + (k_2 + k_3)i_{a2}M_2\cos(\varphi_2)}{4k_2} + \frac{(k_2 - k_3)i_{a1}M_2\cos(\theta + \varphi_1) + (k_2 - k_1)i_{a2}M_1\cos(\theta - \varphi_2)}{4k_2}. \quad (24)$$

The capacitor voltage fluctuations can be easily calculated by integrating corresponding ac components in the capacitor current, and the capacitor voltages in upper, middle, and lower arms can then be calculated as follows:

$$u_{c\_Ua}(t) = U_{c0} + \frac{1}{C}\int i_{c\_Ua}(t)\,dt = u_{c\_\text{dc}} + u_{c\_Ua\_1\omega} + u_{c\_Ua\_2\omega} \tag{25}$$

$$u_{c\_Ma}(t) = U_{c0} + \frac{1}{C}\int i_{c\_Ma}(t)\,dt = u_{c\_\text{dc}} + u_{c\_Ma\_1\omega} + u_{c\_Ma\_2\omega} \tag{26}$$

$$u_{c\_La}(t) = U_{c0} + \frac{1}{C}\int i_{c\_La}(t)\,dt = u_{c\_\text{dc}} + u_{c\_La\_1\omega} + u_{c\_La\_2\omega} \tag{27}$$

where $u_{c\_Ua\_1\omega}$, $u_{c\_Ua\_2\omega}$, $u_{c\_Ma\_1\omega}$, $u_{c\_Ma\_2\omega}$, $u_{c\_La\_1\omega}$, and $u_{c\_La\_2\omega}$ are the capacitor voltage fluctuations in upper, middle, and lower arms, respectively, whose detailed expressions are shown in Appendix B.

In conventional MMC, fundamental-frequency capacitor voltage fluctuations in upper and lower arms are with the same amplitude but opposite phase, while their double-frequency capacitor voltage fluctuations are with the same phase and amplitude [20], [21]. As shown in Appendix B, although capacitor voltage fluctuations in 9A-MMC are still composed of fundamental-, and double-frequency components, the same regularity as the conventional MMC is no longer observed. In 9A-MMC, the fundamental-frequency capacitor voltage fluctuations in upper and lower arms are still with the opposite phase but different amplitude, while their double-frequency capacitor voltage fluctuations are with the same phase and different amplitude. Besides the analysis for upper and lower arms, the capacitor voltage fluctuations in middle arm are formed by fundamental-, and double-frequency components as well.

The output voltage of SM can be obtained by multiplying the corresponding capacitor voltage with switching function, and the arm voltage is the summation of these SMs' output voltages, which can be given as follows:

$$u_{Ua}(t) = k_1 u_{\text{SM}\_Ua}(t) = k_1 f_{Ua}(t) u_{c\_Ua}(t) \tag{28}$$

$$u_{Ma}(t) = k_2 u_{\text{SM}\_Ma}(t) = k_2 f_{Ma}(t) u_{c\_Ma}(t) \tag{29}$$

$$u_{La}(t) = k_3 u_{\text{SM}\_La}(t) = k_3 f_{La}(t) u_{c\_La}(t) \tag{30}$$

where u_{SM_Ua}, u_{SM_Ma}, and u_{SM_La} are the output voltages of SMs in upper, middle, and lower arms.

The voltage ripples of one leg in conventional MMC are the difference between the voltage of one leg and dc-side, which can generate the circulating current [21]. While, the voltage ripples of one leg in 9A-MMC can be expressed as follows:

$$u_{unba}(t) = [u_{Ua}(t) + u_{Ma}(t) + u_{La}(t)] - \frac{(k_1 + k_2 + k_3)}{2}U_c = u_{\text{leg}\_1\omega} + u_{\text{leg}\_2\omega} + u_{\text{leg}\_3\omega} \tag{31}$$

where $u_{leg\_1\omega}$, $u_{leg\_2\omega}$, and $u_{leg\_3\omega}$ are the voltage ripples of one leg in 9A-MMC, whose detailed expressions are shown in Appendix C.

It has been proved that the voltage ripples of one leg in conventional MMC consist of only even-frequency fluctuation components, so its circulating current just consists of even-frequency harmonics, in which the second-order negative-sequence harmonic is the major component [20], [21]. As expressed in (31), the voltage ripples of one leg in 9A-MMC consist of fundamental-, double-, and triple-frequency components. Therefore, there are fundamental-, double-, and triple-frequency components in circulating current of 9A-MMC.

The aforementioned analyses are derived based on the ideal condition that ac components of circulating current are neglected and only dc component is considered. If the ac components of circulating current are initially assumed to exist in arm current, and repeating the above analysis process, it can be obtained that circulating current in 9A-MMC contains both odd- and even-frequency components, where the fundamental-, double-, and triple-frequency harmonic components are dominant. The *n*th-order harmonic components in circulating current can be calculated by *n*th-order voltage ripple in one leg, which can be expressed as follows:

$$i^n_{zj}(t) = \frac{u^n_{unbj}(t)}{jn\omega 2L_{\text{arm}}}. \tag{32}$$

Then, the whole circulating current in 9A-MMC can be expressed as follows:

$$i_{zj}(t) = \frac{1}{3}I_{\text{dc}} + \sum_{n=1}^{+\infty} i^{(n)}_{zj} \sin(n\omega t + \varphi_{zn}) \tag{33}$$

where $i^{(n)}_{zj}$ and φ_{zn} are the amplitude and phase angle of *n*th-order harmonic circulating current.

The above analyses are established by assuming the operation frequencies of two sets of output terminals are identical. When 9A-MMC operates under the different frequency mode, the capacitor voltage fluctuations and the voltage ripples of one phase leg can still be derived by repeating the above analysis process, whose detailed expressions are shown in Appendixes D and E, respectively. It is shown that the capacitor voltage fluctuations in upper arm contain ω_1, ω_2, $2\omega_1$, and $(\omega_2 \pm \omega_1)$ frequency components, the capacitor voltage fluctuations in middle arm contain $\omega_1, \omega_2, 2\omega_1, 2\omega_2$, and $(\omega_2 \pm \omega_1)$ frequency components, and the capacitor voltage fluctuations in lower arm contain ω_1, ω_2, $2\omega_2$, and $(\omega_2 \pm \omega_1)$ frequency components. As the voltage ripples of one phase leg contain ω_1, ω_2, $2\omega_1$, $2\omega_2$, $3\omega_1$, $3\omega_2$, $(\omega_2 \pm \omega_1)$, $(\omega_2 \pm 2\omega_1)$, and $(2\omega_2 \pm \omega_1)$ frequency components, the harmonic components of circulating current would also contain ω_1, ω_2, $2\omega_1$, $2\omega_2$, $3\omega_1$, $3\omega_2$, $(\omega_2 \pm \omega_1)$, $(\omega_2 \pm 2\omega_1)$, and $(2\omega_2 \pm \omega_1)$ frequency components. Besides, the different frequency operation mode will need more SMs for the middle arm, which will make the advantage of 9A-MMC not obvious. Therefore, the different frequency operation mode of 9A-MMC will not be elaborated in this article.

III. OPERATIONAL ANALYSES OF 9A-MMC

The one phase configuration of 9A-MMC is shown in Fig. 4 for easy analysis, where identically constructed half-bridge SMs

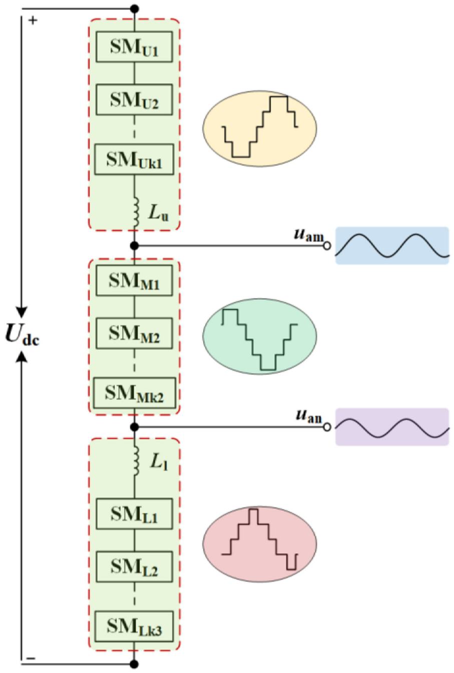

Fig. 4. Illustration of one phase 9A-MMC.

are used in each arm to generate the multilevel stepped waveforms. According to the operational principle of half-bridge SM, its output voltage is either 0 or the capacitor voltage U_c, which depends on the states of its upper and lower switches. The arm voltage is formed by these SMs' output voltage, so the range of upper arm voltage is from 0 to k_1U_c, the middle arm voltage is from 0 to k_2U_c, and the lower arm voltage is from 0 to k_3U_c.

To generate the desired three-phase output voltage, the arm voltage should be controlled to follow a proper reference voltage. By adopting the phase-shifted carrier-based pulsewidth modulation (PSC-PWM), the number of SMs inserted into per arm can be determined, and Fig. 5 demonstrates the change of the activated SMs' number and output voltage level with the variations of arm reference voltage. For ease of understanding, the case that $k_1 = k_2 = k_3 = 4$ is considered. The modulation ratios of upper and lower output terminal are set as 1.0 and 0.8, and phase shift between two output terminals is fixed at 60°.

A. Operation Range Analyses of 9A-MMC

The upper, middle, and lower arm reference voltages can be calculated by (1)–(3), and the normalized arm reference voltage of phase A can be expressed as follows:

$$u_{Ua}(t) = \frac{1}{2}\left[1 - M_1 \sin(\omega t)\right] \tag{34}$$

$$u_{Ma}(t) = \frac{1}{2}\left[1 + \frac{k_1}{k_2} M_1 \sin(\omega t) - \frac{k_3}{k_2} M_2 \sin(\omega t + \theta)\right] \tag{35}$$

$$u_{La}(t) = \frac{1}{2}\left[1 + M_2 \sin(\omega t + \theta)\right]. \tag{36}$$

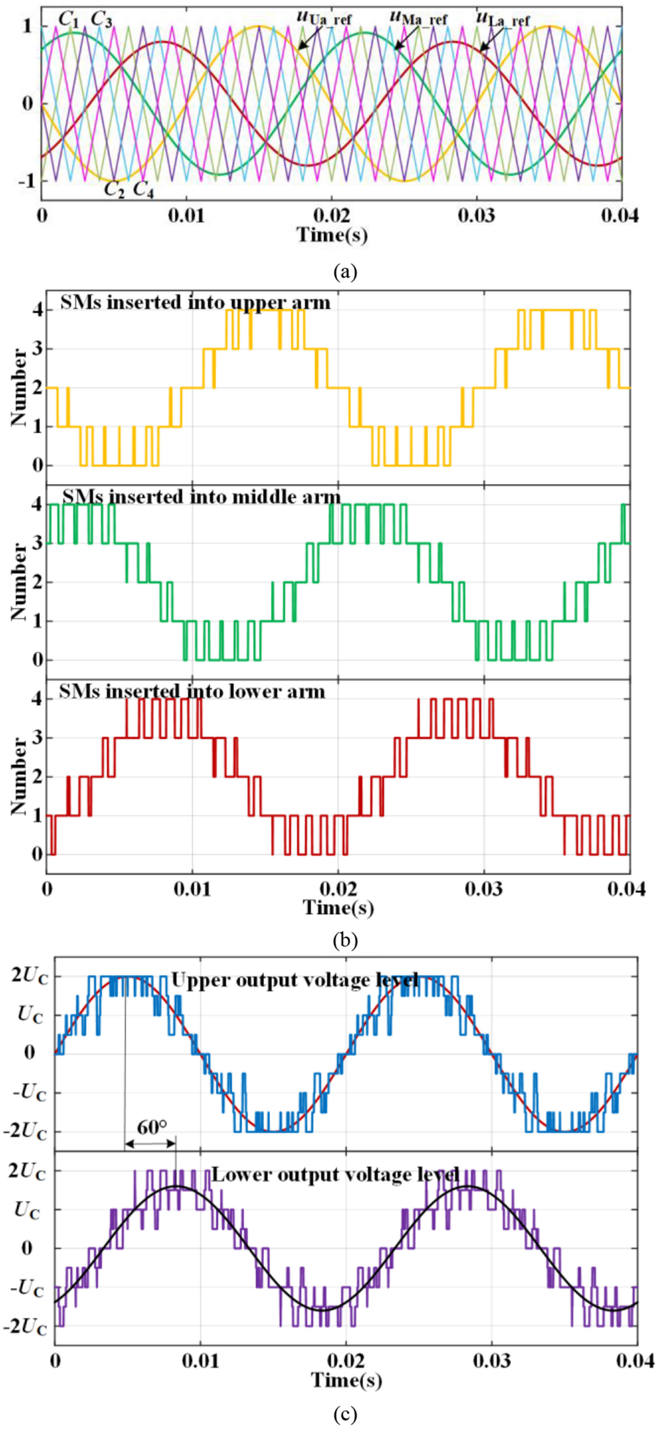

(a)

(b)

(c)

Fig. 5. (a) Modulation references and triangular signals with $M_1 = 1.0$, $M_2 = 0.8$, $\theta = 60°$, and $N = 4$. (b) Number of SMs inserted into upper, middle, and lower arms. (c) Upper and lower output voltages.

According to the operational principle analyses of 9A-MMC, the upper, middle, and lower arm voltages are unipolar, and they are always positive. Hence, the arm reference voltage must be positive at any time. If this condition is not abided, the transferred active power between ac-side and dc-side will be unbalanced, and the capacitor voltage will increase or decrease continuously.

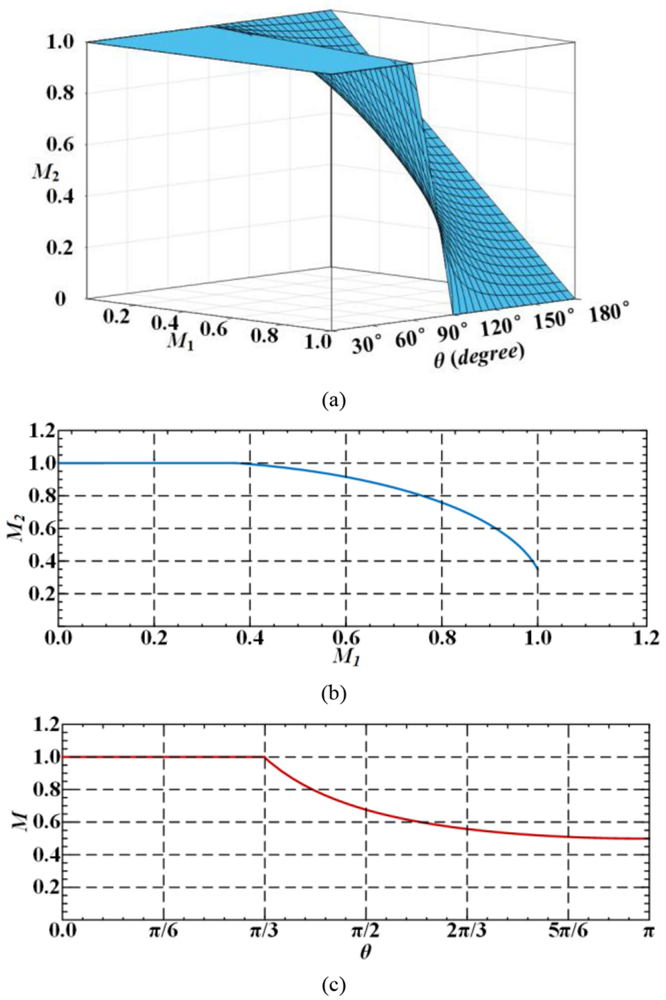

(a)

(b)

(c)

Fig. 6. (a) Relationships among maximum M_1, M_2, and θ. (b) Variations between maximum M_1 and M_2 when θ is fixed at 80°. (c) Variations of maximum $M = M_1 = M_2$ with θ changes from 0° to 180°.

Eventually, the normal operation of 9A-MMC will collapse. Equations (34) and (36) are always positive at any instant, because the range of both M_1 and M_2 is from 0 to 1. As for standard 9A-MMC which uses the same number of SMs in each arm, (35) is not always positive, and can be negative sometimes, which depends on the value of M_1, M_2, and θ. This means that the operation range of standard 9A-MMC will be limited.

To directly illustrate the reasonable operation range of standard 9A-MMC, the three-dimensional (3-D) curves of maximum M_1, M_2, and θ are shown in Fig. 6(a). For clarity, the corresponding 2-D curves between maximum M_1 and M_2 is shown in Fig. 6(b), when θ is set as 80°. Furthermore, to show the influence of θ, the variations of maximum $M = M_1 = M_2$ and θ are shown in Fig. 6(c). As shown in Fig. 6, the values of maximum M_1, M_2, and θ cannot be set arbitrarily, and there are strict restrictions among them. However, considering the number of SMs in three arms can be variable and different, the limitation to the operation range of standard 9A-MMC can be eliminated. Because, for specific M_1, M_2, and θ, (35) can always be positive by elaborately selecting the value of k_1, k_2, and k_3.

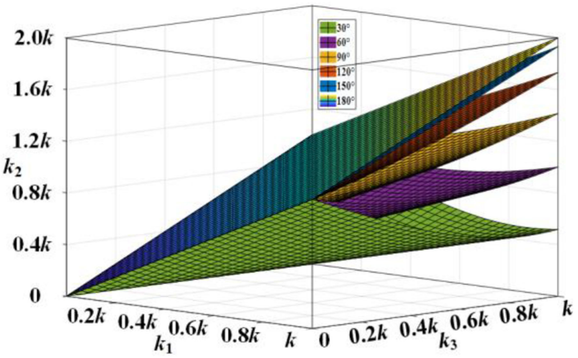

Fig. 7. Relationships among k_1, k_2, and k_3 under the different phase shift θ.

B. Principle of Determining k_1, k_2, and k_3

In principle, k_1 depends on the amplitude of upper output terminal and the rated voltage of SM capacitor, while k_3 depends on the amplitude of lower output terminal and the rated voltage of SM capacitor. They can be calculated as follows:

$$k_1 = ceil\left[\frac{2u_{a1}}{U_c}\right] \tag{37}$$

$$k_3 = ceil\left[\frac{2u_{a2}}{U_c}\right] \tag{38}$$

where *ceil* is the top integral function. Being different, k_2 depends on not only the amplitude of both upper and lower output terminals but also the phase shift between upper and lower output. So, k_2 can be expressed as follows:

$$k_2 = ceil\left[\sqrt{\{k_1M_1 - k_3M_2\cos(\theta)\}^2 + \{k_3M_2\sin(\theta)\}^2}\right]. \tag{39}$$

For convenience of analysis, the case that the number of SMs in upper and lower arms is equal to k is taken as a criterion, and the 3-D curves of variations among k_1, k_2, and k_3 under different phase shift θ is shown in Fig. 7.

IV. CONTROL SCHEME OF 9A-MMC

The whole control diagram of 9A-MMC is illustrated in Fig. 8, which is mainly composed of CVBC and CCSC. Moreover, the decoupled voltage control is adopted to generate the fundamental modulation reference.

There are various modulation methods suitable for conventional MMC. Among different modulation techniques, PSC-PWM is developed to generate switching signals for 9A-MMC in this article, due to its capacitor voltage self-balancing capability and high effective switching frequency [22], [23]. In PSC-PWM technique, each SM is controlled independently, and in total k_1, k_2, k_3 triangular carriers with phase shifted by $2\pi/k_1$, $2\pi/k_2$, $2\pi/k_3$ for upper, middle and lower arms are required, respectively. Then, the comparison between SM modulation reference and triangular carriers produces the corresponding SM switching signals.

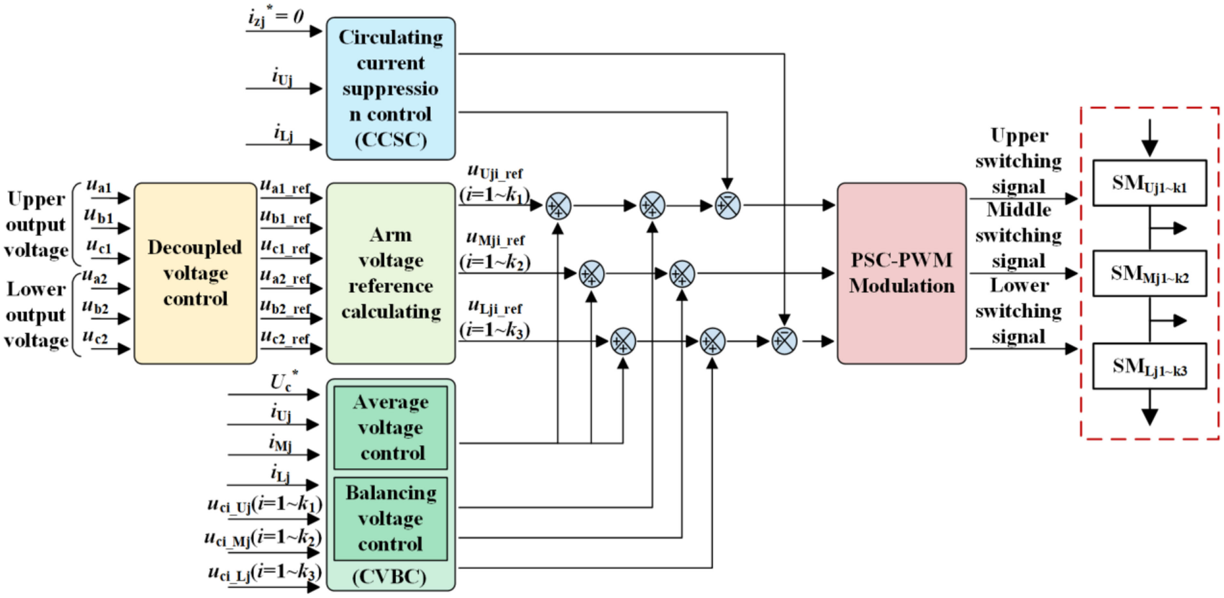

Fig. 8. Whole control scheme of 9A-MMC.

A. Capacitor Voltage Balancing Control

Capacitor voltage balancing is the primary control objective for normal operation of 9A-MMC, and CVBC in PSC-PWM technique is usually separated into average voltage control and balancing voltage control [24].

1) Average Voltage Control: The average capacitor voltage in one leg can be calculated as follows:

$$\overline{U}_{cj} = \frac{1}{3(k_1 + k_2 + k_3)} \times \left(\sum_{i=1}^{k_1} u_{ci\_Uj} + \sum_{i=1}^{k_2} u_{ci\_Mj} + \sum_{i=1}^{k_3} u_{ci\_Mj} \right) \tag{40}$$

where u_{ci_Uj}, u_{ci_Mj}, and u_{ci_Lj} are the measured ith capacitor voltage of upper, middle, and lower arm, respectively.

Average voltage control can regulate average capacitor voltage in one leg, which is realized by adjusting the dc component in circulating current. As shown in Fig. 9(a), average voltage control has two control loops, one is outer voltage control, and another is inner current control. In specific, the outer voltage control can minimize the error between capacitor voltage reference U_c^* and average capacitor voltage of one leg by using a proportional integral (PI) controller, then it gives the reference of dc component in circulating current. The inner current control can minimize the error between the command of dc component in circulating current and the measured circulating current by employing another PI controller, then it gives a compensating signal, which will be added into the fundamental modulation reference generated by the decoupled voltage control.

2) Balancing Voltage Control: The balancing voltage control in PSC-PWM, which is mainly to balance the capacitor voltage in the same arm, is usually implemented prior to the modulation stage and distributed in each SM. As shown in Fig. 9(b), the error between the capacitor voltage reference U_c^* and the measured capacitor voltage is regulated by the PI controller, then the compensation signal for each SM can be obtained. This compensation signal will be also added into the modulation reference of each SM. Besides, the polarity of the final compensation signal depends on the polarity of arm current.

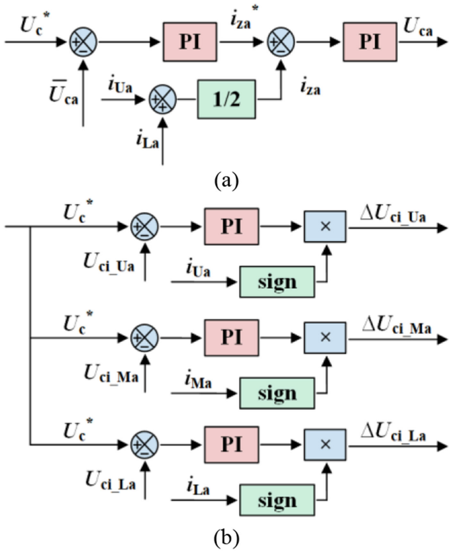

Fig. 9. Block diagram of (a) average voltage control and (b) balancing voltage control.

B. Circulating Current Suppression Control

The circulating current only flows through three-phase units without impacting the dc-side current, and it is dominated by the negative-sequence second-order harmonics current in conventional MMC [25], [26]. Although circulating current

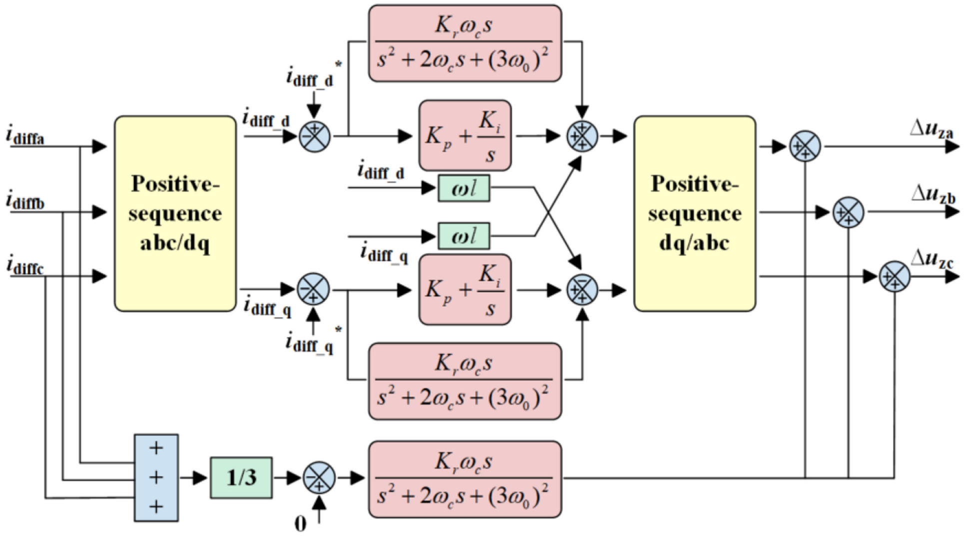

Fig. 10. Block diagram of the circulating current suppression controller.

control can be regarded as secondary objective under normal operation of MMC, if not suppressed, circulating current can increase the peak value of arm current, which can lead to high current stress, large converter losses, and large SM capacitor voltage ripples [27]. Hence, the CCSC is usually included into the whole control scheme, and CCSC in conventional MMC is designed mainly to mitigate the second-frequency components of circulating current. However, according to the previous analyses, circulating current in 9A-MMC consists of both odd- and even-frequency harmonics, where the fundamental-, double- and, triple-frequency components are dominant. Besides, zero-sequence components of circulating current can flow through dc side and distort the dc-side current. Hence, CCSC adopted in conventional MMC is no longer suitable for 9A-MMC unless several PI controllers in multiple rotating reference frames or PR controllers in the stationary reference frame are employed. However, such solution is complex and will unavoidably increase the calculation burden. Therefore, a novel CCSC method based on the proportional integral resonant (PIR) controller is proposed to simultaneously suppress multiple-frequency harmonic components in circulating current of 9A-MMC. As shown in Fig. 10, the proposed CCSC method consists of PI controller and third harmonic resonant controller. Although resonant controller can be effectively used in the stationary reference frame, it has the capability of compensating two harmonics at the same time in rotating reference frames [28]. Therefore, the PIR controller adopted in the proposed CCSC method is plugged into rotating reference frames in order to compensate both second-order and fourth-order harmonics. According to the circulating currents analyses, the second-order harmonic in circulating current is a negative-sequence current, the third-order harmonic component is a zero-sequence current, and the fourth-order harmonic component is a positive-sequence current. Thus, if adopting a positive-sequence rotating reference frames rotating at fundamental frequency, the first-order harmonic in circulating currents can be transformed into dc components, meanwhile second- and fourth-order harmonics can be transformed into third-order harmonic components. So, the designed PIR controller can synchronously suppress first-, second-, and fourth-order harmonics in circulating current. Another third harmonic resonant controller is used to suppress third-order zero-sequence harmonic in circulating current. Finally, the sum of compensation signals generated by PIR controller only needs to be added into SM modulation reference in upper and lower arm. Besides, because the quasi-resonant controller can obtain wider bandwidth in the real application in which the frequency deviation may happen [29], the quasi-resonant controller is adopted in the proposed CCSC method.

In summary, the final modulation reference for each SM in upper, middle, and lower arms can be expressed as follows:

$$u_{i\_Uj} = \frac{1}{2} - u_{j1\_\mathrm{ref}} + u_{cj} + \Delta u_{ci\_Uj} - \Delta u_{zj} \tag{41}$$

$$u_{i\_Mj} = \frac{1}{2} + \frac{k_1}{k_2} u_{j1\_\mathrm{ref}} - \frac{k_3}{k_2} u_{j2\_\mathrm{ref}} + u_{cj} + \Delta u_{ci\_Mj} \tag{42}$$

$$u_{i\_Lj} = \frac{1}{2} + u_{j2\_\mathrm{ref}} + u_{cj} + \Delta u_{ci\_Lj} - \Delta u_{zj} \tag{43}$$

where u_{j1_ref} and u_{j2_ref} are the upper and lower output voltage control commands determined by the decoupled voltage control, respectively. u_{cj}, Δu_{ci_Uj}, Δu_{ci_Mj}, and Δu_{ci_Lj} are the compensation signals generated by CVBC, Δu_{zj} is the compensation signal generated by CCSC. The detailed control diagrams of decoupled voltage control are shown in Fig. 11, which are conventional and will not be further elaborated.

V. COMPARISONS BETWEEN 9A-MMC AND CONVENTIONAL MMCS

The comparisons including the number of required SM, SM capacitors, insulated gate bipolar transistors (IGBTs), diodes, corresponding gate-drive circuits, and capacitor voltage sensors between 9A-MMC and two conventional MMCs are investigated in this section. To clearly demonstrate the advantage of 9A-MMC for reducing components, Fig. 12 shows graphic

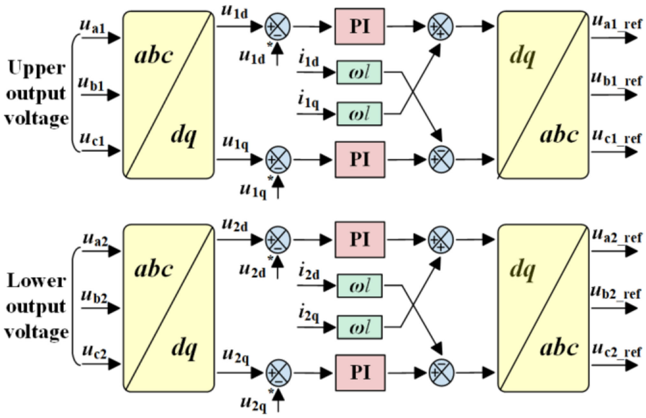

Fig. 11. Block diagrams of the decoupled voltage control.

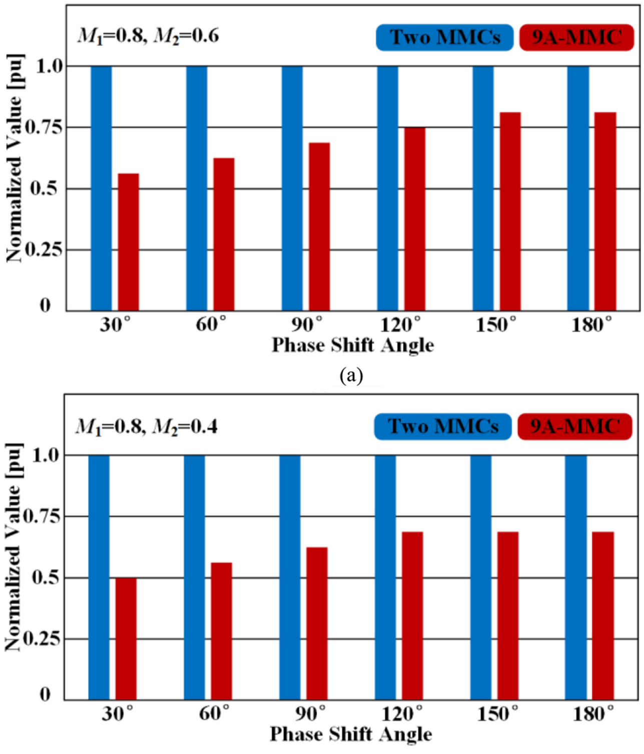

(a)

(b)

Fig. 12. Comparisons of components count between two conventional MMCs and 9A-MMC when the modulation ratios of two sets of output terminals are set as (a) 0.8 and 0.6, (b) 0.8 and 0.4.

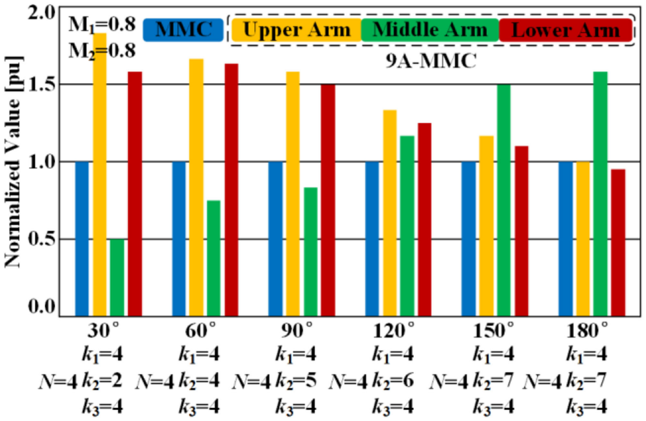

Fig. 13. Comparisons of the maximum capacitor voltage ripple between conventional MMC and 9A-MMC with the phase shift angle (i.e., the SM numbers) variation.

comparisons of the required components between 9A-MMC and conventional MMC under different output voltage amplitudes and phase shift angles, where the number of required components in two conventional MMCs is taken as the reference. In specific, Fig. 12(a) and (b) display the comparisons when the modulation ratios of two sets of three-phase terminals are set as 0.8 and 0.6, 0.8 and 0.4, respectively, and the phase shift angle changes from 30° to 180°.

It is noted that the normalized comparisons shown in Fig. 12 can represent the comparative device counts of required SM, SM capacitors, IGBTs, diodes, gate-drive circuits, or capacitor voltage sensors. Obviously, the number of required components in 9A-MMC can be dramatically reduced compared with two conventional MMCs. Moreover, compared with two conventional MMCs, the further reduction of required components count in 9A-MMC can be obtained when the modulation ratios of two sets of output terminals have the large difference.

In [21], the capacitor voltage ripples of conventional MMC have been investigated in detail, which mainly consist of the first- and second-order ripple components. While, the capacitor voltage ripples of 9A-MMC can be calculated according to (B1)–(B6) shown in Appendix B, which mainly consist of the first- and second-order ripple components as well. Generally, the SM capacitance is determined by the maximum capacitor voltage ripple. Therefore, Fig. 13 shows the comparisons of the maximum capacitor voltage ripple between conventional MMC and 9A-MMC under different application scenarios, where only the first- and second-order capacitor voltage ripples are taken into account, and the maximum capacitor voltage ripple in conventional MMC is used as the reference for comparison.

It is observed that the maximum capacitor voltage ripples of upper and lower arms in 9A-MMC are reduced, but the maximum capacitor voltage ripple of middle arm is increased when the modulation ratio of both upper and lower output terminal is fixed as 0.8 and the phase shift angle between them (i.e., the SM number) increases. Besides, the maximum capacitor voltage ripple is constant in conventional MMC. While, the maximum capacitor voltage ripple of 9A-MMC would be larger than that of conventional MMC in some application scenarios as indicated in Fig. 13. Therefore, to keep the same maximum capacitor voltage ripple, the SM capacitance of 9A-MMC would be larger than that of conventional MMC. This is because two sets of output currents simultaneously flow through the arms of 9A-MMC, however, the arm currents of conventional MMC only contain one set of output currents.

VI. SIMULATION RESULTS

To verify the performance of 9A-MMC and the proposed control scheme, the simulation is carried out in MATLAB/Simulink

TABLE I
SIMULATION PARAMETERS FOR 9A-MMC

Parameters	Value
SM capacitor voltage U_c	200 V
SM capacitor C	1 mF
Fundamental frequency f	50 Hz
Carrier frequency f_c	5000 Hz
Arm inductor L_{arm}	2 mH

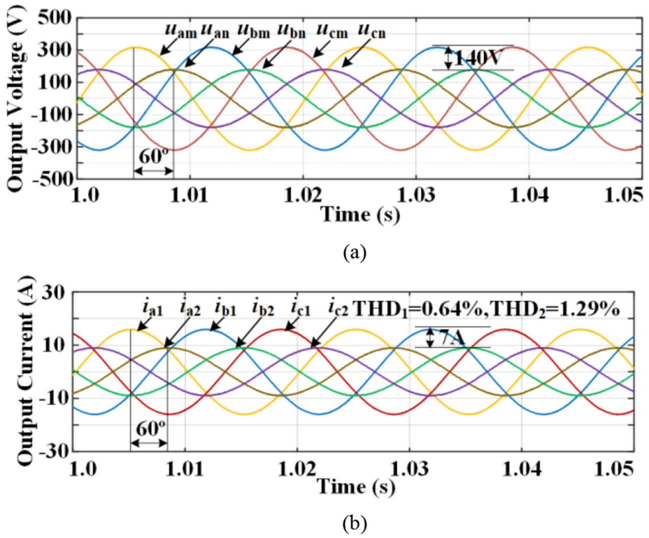

(a)

(b)

Fig. 14. (a) Output voltages of upper and lower terminals. (b) Output currents of upper and lower terminals.

to power two identical inductive loads with $L = 5$ mH and $R = 20\ \Omega$. The dc side of 9A-MMC is connected to a pure dc source. The key simulation parameters for 9A-MMC are listed in Table I.

The simulation results under two different output targets are sequentially presented. The first output target is that the amplitude of upper and lower output terminal is respectively set as 320 and 180 V, and the phase shift between them is set as 60°. The second output target is that the amplitude of both upper and lower output terminal is set as 320 V, and the phase of lower output terminal is shifted by 80° behind the upper output terminal. According to (37)–(39) in Section III, k_1, k_2, and k_3 for the first output target are 4, 3, and 2, while k_1, k_2, and k_3 for the second output target are 4, 5, and 4.

1) *Case 1.* $u_{jm} = 320$ V, $u_{jn} = 180$ V, $\Delta\theta = 60°$: The upper and lower output voltages (u_{am}, u_{bm}, u_{cm} and u_{an}, u_{bn}, u_{cn}) and currents (i_{a1}, i_{b1}, i_{c1} and i_{a2}, i_{b2}, i_{c2}) are shown in Fig. 14(a) and (b). It is obvious that the upper and lower output currents are standard sinusoidal waveforms with the THD of 0.64% and 1.29%, respectively. Fig. 15 presents the upper, middle, and lower arm voltages with $k_1 = 4$, $k_2 = 3$, $k_3 = 2$. The circulating currents (i_{za}, i_{zb}, i_{zc}) without and with CCSC are shown in Fig. 16(a), and the corresponding spectrum of circulating currents in phase A without and with CCSC are shown in Fig. 16(b).

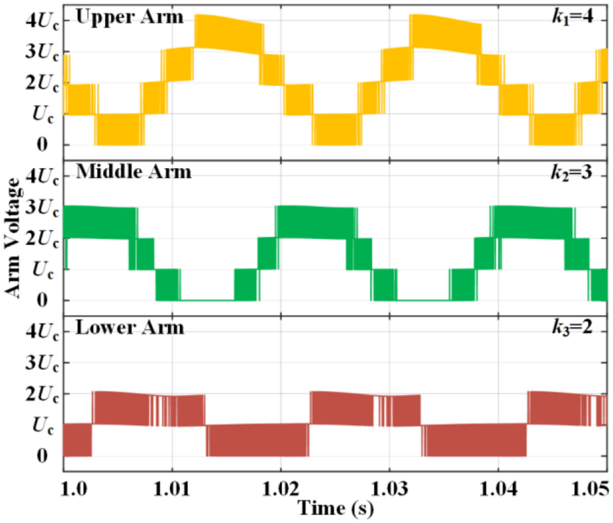

Fig. 15. Upper, middle, and lower arm voltages with $k_1 = 4$, $k_2 = 3$, $k_3 = 2$.

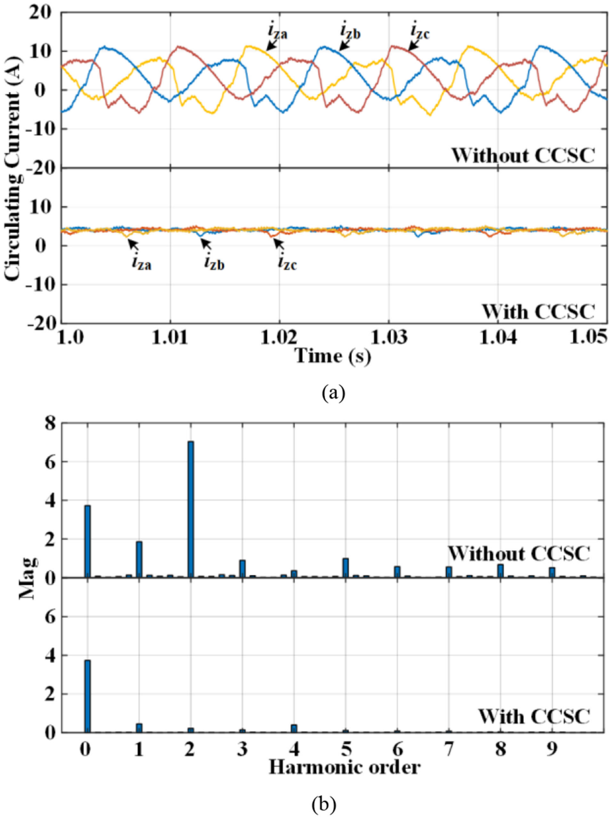

(a)

(b)

Fig. 16. (a) Circulating currents without and with CCSC. (b) Spectrum of circulating currents in phase A without and with CCSC.

Comparing the circulating currents without and with CCSC in Fig. 16(a), the peak-to-peak ripple of circulating current is reduced from 15 to 1.3 A. And according to the spectrum of circulating currents without CCSC shown in Fig. 16(b), the fundamental-, double-, and triple-frequency components are dominant in circulating currents, which is consistent with the mathematical analyses. As shown in the bottom of Fig. 16(b),

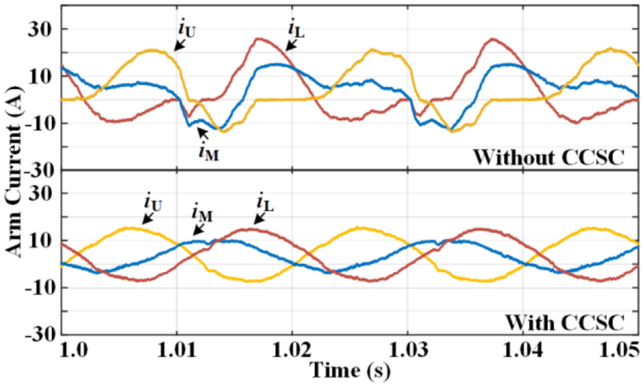

Fig. 17. Arm currents in phase A without and with CCSC.

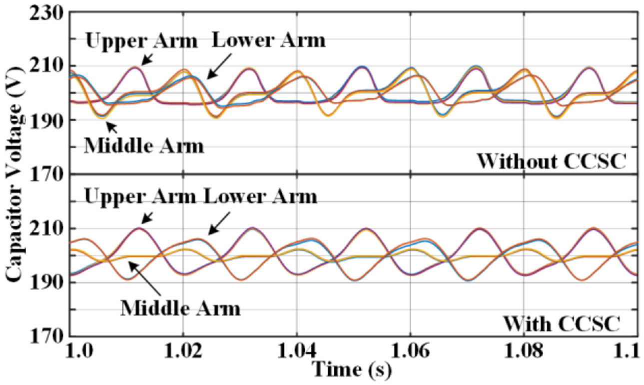

Fig. 18. Capacitor voltages in upper, middle, and lower arm without and with CCSC.

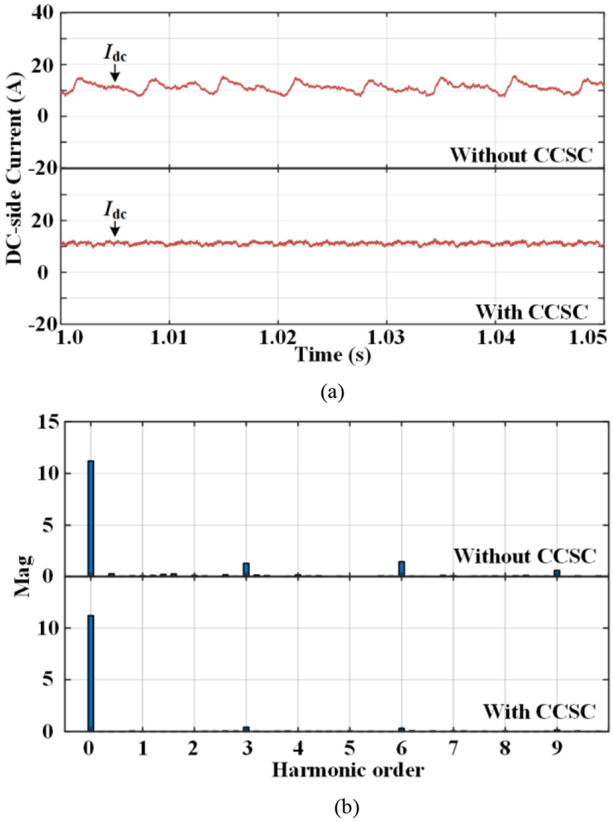

(a)

(b)

Fig. 19. (a) DC-side current without and with CCSC. (b) Spectrum of dc-side current without and with CCSC.

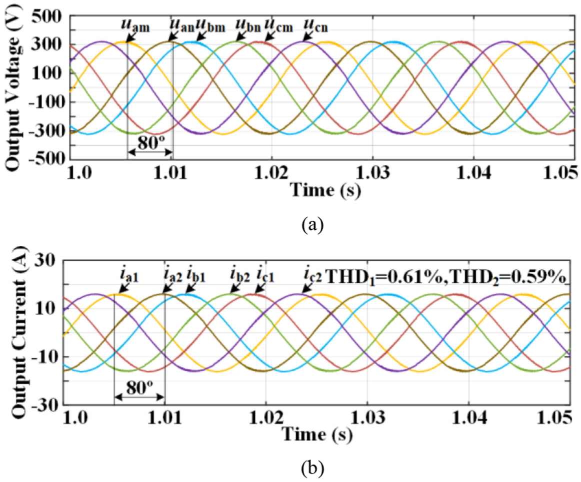

(a)

(b)

Fig. 20. (a) Output voltages of upper and lower terminal. (b) Output currents of upper and lower terminal.

it is observed that the dominant harmonic components of circulating current are suppressed effectively by the proposed CCSC method. Fig. 17 displays the arm currents (i_{Ua}, i_{Ma}, i_{La}) without and with CCSC. It can be seen that the distortion of arm currents shown in the bottom of Fig. 17 is mitigated by CCSC. Also, all capacitor voltages in upper, middle, and lower arms shown in Fig. 18 are balanced at 200 V as expected, which is benefited from the CVBC method in this article. The dc-side current (I_{dc}) without and with CCSC are shown in Fig. 19(a), and the corresponding spectrum of I_{dc} without and with CCSC are shown in Fig. 19(b). Due to the existence of circulating currents, I_{dc} shown in the top of Fig. 19(a) is distorted. The spectrum of I_{dc} without CCSC shows that I_{dc} consists of zero-sequence circulating currents, such as 3th-, 6th-, and 9th-order harmonics, while the distortion of I_{dc} can be mitigated by the CCSC method presented in this article as shown in Fig. 19(a) and (b).

2) *Case 2.* $u_{jm} = 320$ V, $u_{jn} = 320$ V, $\Delta\theta = 80°$: Fig. 20(a) records the upper and lower output voltages (u_{am}, u_{bm}, u_{cm} and u_{an}, u_{bn}, u_{cn}), meanwhile Fig. 20(b) shows the upper and lower output currents (i_{a1}, i_{b1}, i_{c1} and i_{a2}, i_{b2}, i_{c2}). It is shown that 9A-MMC can also output perfect waveforms under this output target. The upper, middle, and lower arm voltages with $k_1 = 4$, $k_2 = 5$, $k_3 = 4$ are shown in Fig. 21. The circulating currents (i_{za}, i_{zb}, i_{zc}) without and with CCSC are displayed in Fig. 22(a), and Fig. 22(b) presents the spectrum of the corresponding circulating current without and with CCSC. It can be observed that the harmonics components of circulating currents are well suppressed. As shown in Fig. 23, the distortion of arm currents (i_U, i_M, i_L) with CCSC is significantly reduced due to the absence of circulating current harmonic components. The capacitor voltages in upper, middle, and lower arms are shown in Fig. 24, and all capacitor voltages can be kept balanced around

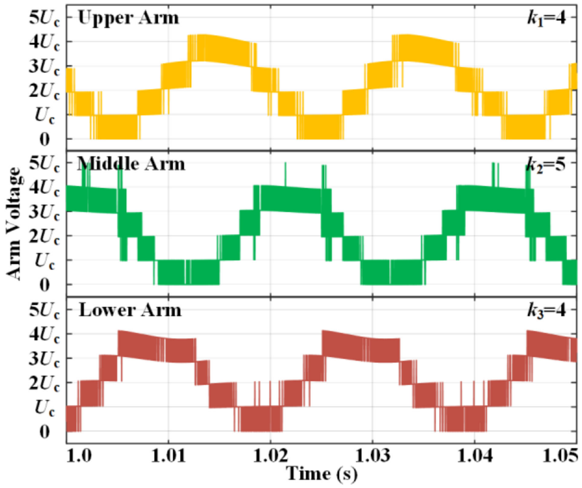

Fig. 21. Upper, middle, and lower arm voltage level with $k_1 = 4$, $k_2 = 5$, $k_3 = 4$.

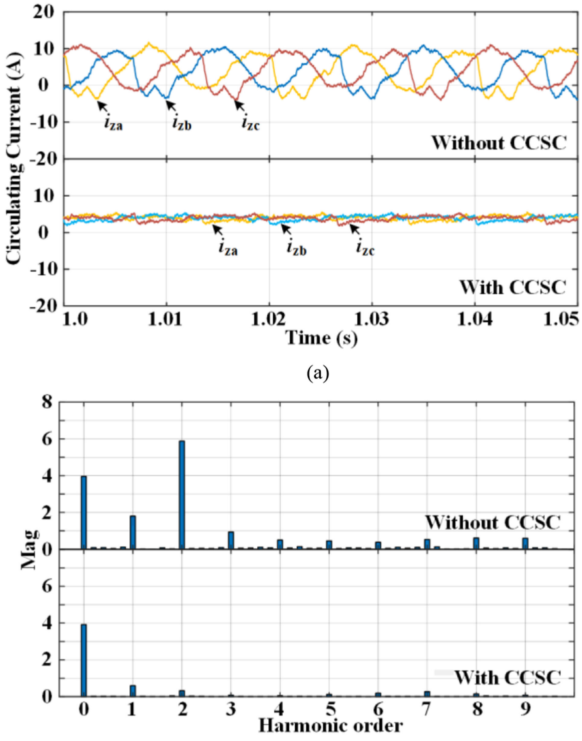

(a)

(b)

Fig. 22. (a) Circulating currents without and with CCSC. (b) Spectrum of circulating currents in phase A without and with CCSC.

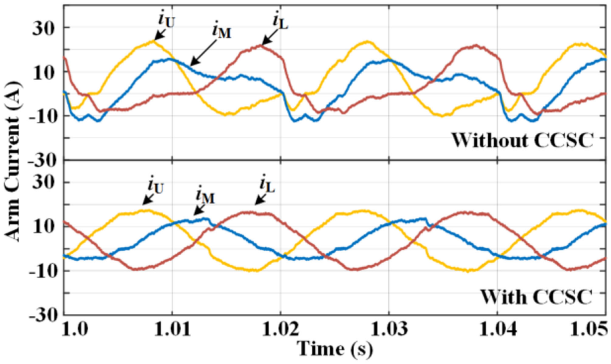

Fig. 23. Arm currents in phase A without and with CCSC.

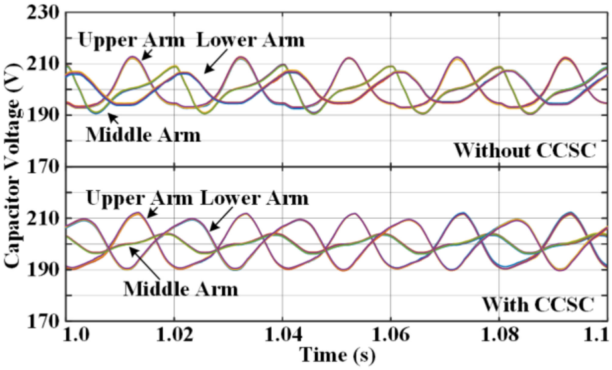

Fig. 24. Capacitor voltages in upper, middle, and lower arm without and with CCSC.

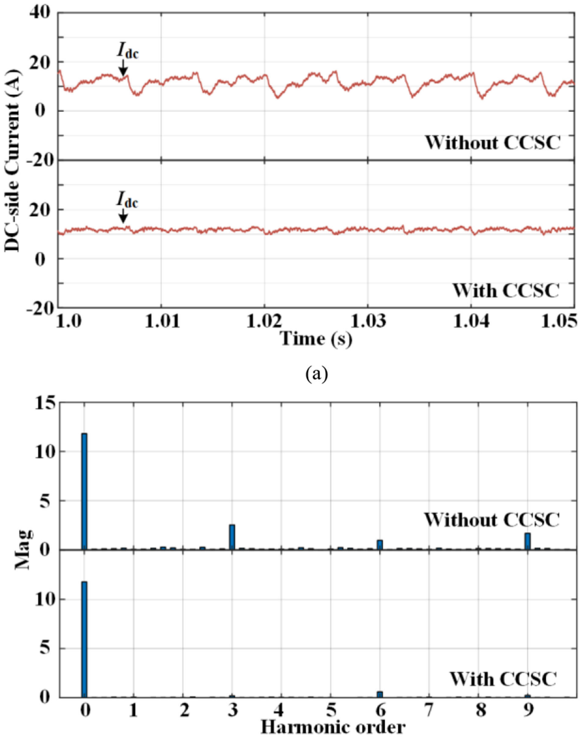

(a)

(b)

Fig. 25. (a) DC-side current without and with CCSC. (b) Spectrum of dc-side current without and with CCSC.

capacitor voltage reference. The dc-side current I_{dc} without and with CCSC and its spectrum are presented in Fig. 25(a) and (b), respectively. It is observed that the proposed control scheme can work well under the above operation scenarios.

VII. EXPERIMENTAL RESULTS

As shown in Fig. 26, a scale-down three-phase prototype of 9A-MMC has been built to further validate the performance of 9A-MMC and the proposed control scheme. The control scheme

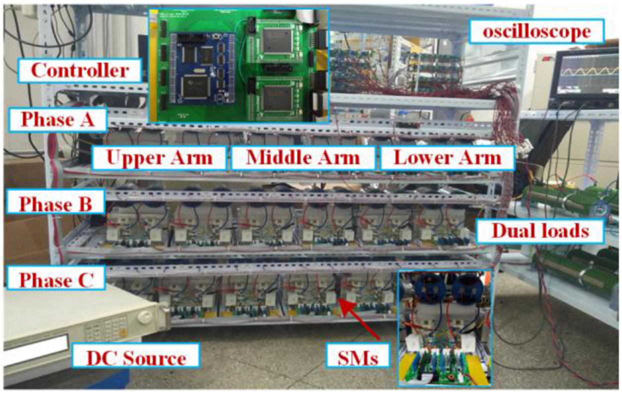

Fig. 26. Photograph of three-phase 9A-MMC prototype.

TABLE II
EXPERIMENTAL PARAMETERS FOR 9A-MMC

Parameters	Value
SM capacitor voltage U_c	50 V
SM capacitor C	520 μF
Fundamental frequency f	50 Hz
Carrier frequency f_c	5000 Hz
Arm inductor L_{arm}	2 mH
Output filter inductor L	5 mH
Loads R	30 Ω

is implemented in a controller consisting of a TMS320F28335 DSP plus two XC3S500E-4PQG208C field programmable gate arrays (FPGAs). The DSP is used to read external AD results and perform most of calculation. Finally, it will provide the modulation reference of each SM. Meanwhile, one FPGA is used to control external AD to obtain the arm currents, capacitor voltages and output status of 9A-MMC, and the other FPGA is used to carry out modulation and send PWM signals for each SM. The detailed experimental parameters are listed in Table II.

Fig. 27 displays the upper and lower output voltages and currents in phase A under two different output targets. The first output target is that the amplitude of upper output terminal is set as 80 V, while the amplitude of lower output terminal is set as 60 V. The phase shift between upper and lower output terminal is set as 60°. The second output target is that the amplitude of both upper and lower output terminals is set as 70 V, and the phase of lower output terminal is shifted by 80° behind the upper output terminal. Besides, according to (37)–(39), k_1, k_2, and k_3 for the first output target are 4, 3, and 3, and k_1, k_2, and k_3 for the second output target are 3, 4, and 3. As shown in Fig. 27, 9A-MMC can output the desired waveforms according to different output targets.

Fig. 28 shows the capacitor voltages in upper, middle, and lower arm and dc-side current. The waveforms in Fig. 28(a) is under the first output target, and the waveforms in Fig. 28(b) is under the second output target. As shown in Fig. 28, the capacitor voltages in each arm can maintain balanced around the capacitor voltage reference, and the harmonic components of dc-side current are successfully mitigated by CCSC method in this article.

Fig. 29 shows the currents in upper, middle, and lower arms and circulating current in phase A. The waveforms under the

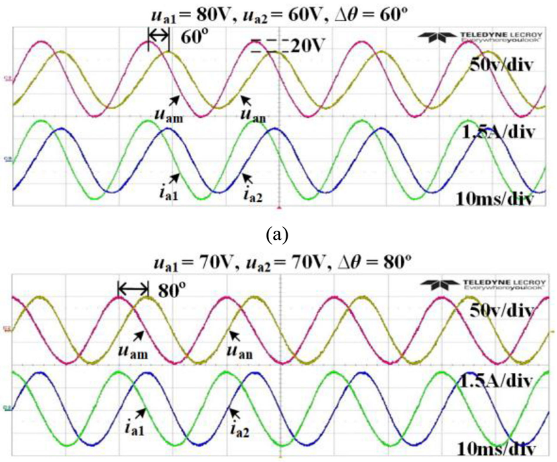

(a)

(b)

Fig. 27. Upper and lower output voltage and current in phase A under (a) the first output target and (b) the second output target.

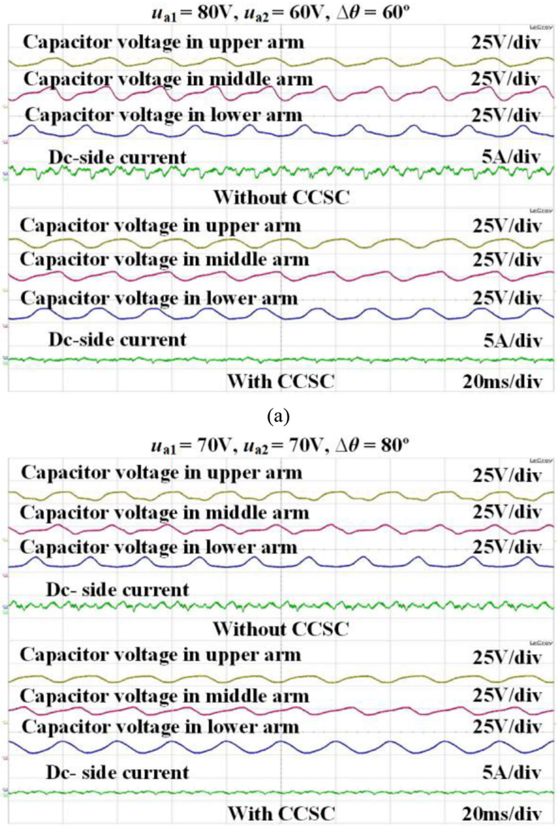

(a)

(b)

Fig. 28. Capacitor voltage in upper, middle, and lower arm and dc-side current without and with CCSC under (a) the first output target and (b) the second output target.

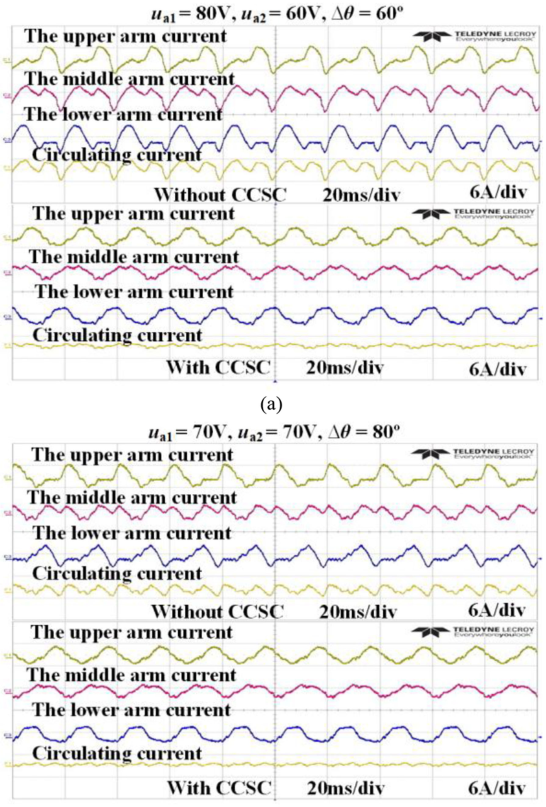

(a)

(b)

Fig. 29. Currents in upper, middle, and lower arm and circulating current without amd with CCSC under (a) the first output target and (b) the second output target.

above output targets are respectively displayed in Fig. 29(a) and (b). As shown in Fig. 29, the arm currents without CCSC are distorted. It is obvious that the circulating current can be effectively suppressed by the proposed CCSC method, and the distortion of arm currents is reduced as well.

The experimental results of output voltages and currents in phase A, arm voltages, capacitor voltages, and circulating current are shown in Fig. 30(a)–(c), respectively, where the converter output changes from one state that the amplitude of both upper and lower output is 70 V and the phase shift angle between them is 60° to another state that the amplitudes of upper and lower output are set as 80 and 50 V, and the phase shift angle between them is still 60°. Meanwhile, the SM numbers of upper, middle, and lower arms change from 3, 3, and 3 to 4, 3, and 2.

In addition, for evaluating the dynamic output performance of 9A-MMC, the amplitude of both upper and lower output voltage is set as 70 V and the phase shift angle between them is fixed as 60°, but the upper load changes from 30 to 20 Ω, and the lower load remains unchanged. Fig. 31 presents the experimental results of the output voltages and currents in phase A, arm voltages, capacitor voltages, and circulating current, respectively.

It is noted that the experimental results are consistent with the theoretical analysis, and validate the unique operation modes of 9A-MMC and the proposed control scheme.

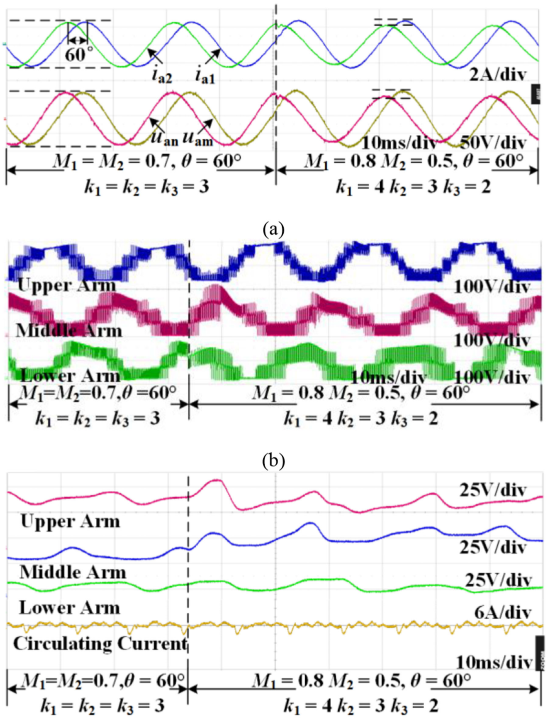

(a)

(b)

(c)

Fig. 30. Experimental results of (a) output voltages and currents in phase A, (b) arm voltages of upper, middle, and lower arms, and (c) capacitor voltages and circulating current when the output state changes.

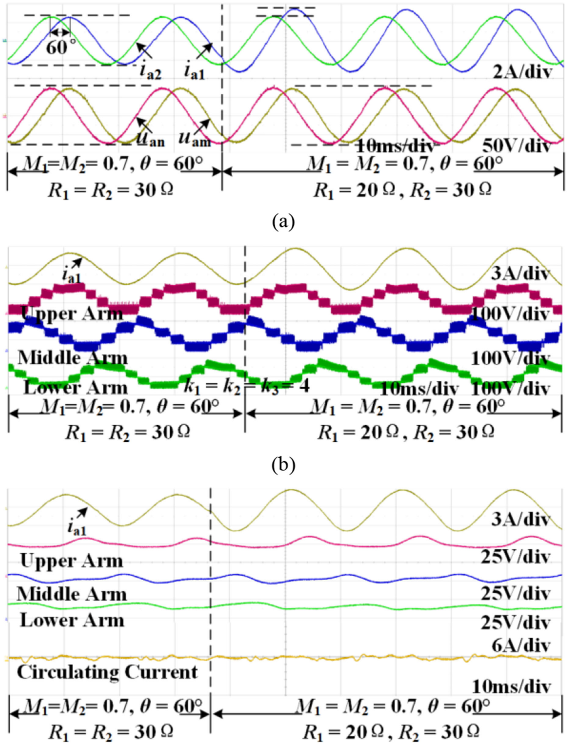

(a)

(b)

(c)

Fig. 31. Experimental results of (a) output voltages and currents in phase A, (b) arm voltages of upper, middle, and lower arm, and (c) capacitor voltages and circulating current under load changing condition.

VIII. CONCLUSION

The mathematical model and detailed operational analyses of 9A-MMC are presented in this article. Furthermore, it is found that the submodule counts in upper, middle, and lower arms can be different in implementation, which is flexible under different operation modes, being different from the standard 9A-MMC. Moreover, the steady-state analyses of capacitor voltage fluctuations and circulating current have been carried out, which reveals that capacitor voltage fluctuations and circulating current in 9A-MMC are different from the conventional MMC. This article then proposes the complete control scheme for 9A-MMC including CVBC and CCSC. Finally, the simulation and experimental results verified the performance of 9A-MMC and the effectiveness of the proposed control scheme.

APPENDIX A

The detailed expressions of $i_{c\_Ua\_\mathrm{dc}}$, $i_{c\_Ua\_1\omega}$, $i_{c\_Ua\_2\omega}$, $i_{c\_Ma\_\mathrm{dc}}$, $i_{c\_Ma\_1\omega}$, $i_{c\_Ma\_2\omega}$, $i_{c\_La\_\mathrm{dc}}$, $i_{c\_La\_1\omega}$, and $i_{c\_La\_2\omega}$ are shown as follows:

$$i_{c\_Ua\_\mathrm{dc}} = \frac{I_{\mathrm{dc}}}{6} - \frac{i_{a1}M_1\cos(\varphi_1)}{8} - \frac{i_{a2}M_1\cos(\theta-\varphi_2)}{8} \tag{A1}$$

$$\begin{aligned} i_{c\_Ua\_1\omega} = &-\frac{I_{\mathrm{dc}}M_1\sin(\omega t)}{6} + \frac{i_{a1}\sin(\omega t-\varphi_1)}{4} \\ &+ \frac{i_{a2}\sin(\omega t+\theta-\varphi_2)}{4} \end{aligned} \tag{A2}$$

$$i_{c\_Ua\_2\omega} = \frac{i_{a1}M_1\cos(2\omega t-\varphi_1)}{8} + \frac{i_{a2}M_1\cos(2\omega t+\theta-\varphi_2)}{8} \tag{A3}$$

$$\begin{aligned} i_{c\_Ma\_\mathrm{dc}} = &\frac{I_{\mathrm{dc}}}{6} - \frac{k_1 i_{a1}M_1\cos(\varphi_1)}{8k_2} + \frac{k_3 i_{a1}M_2\cos(\theta+\varphi_1)}{8k_2} \\ &+ \frac{k_1 i_{a2}M_1\cos(\theta-\varphi_2)}{8k_2} - \frac{k_3 i_{a2}M_2\cos(\varphi_2)}{8k_2} \end{aligned} \tag{A4}$$

$$\begin{aligned} i_{c\_Ma\_1\omega} = &\frac{k_1 I_{\mathrm{dc}}M_1\sin(\omega t)}{6k_2} - \frac{k_3 I_{\mathrm{dc}}M_2\sin(\omega t+\theta)}{6k_2} \\ &- \frac{i_{a1}\sin(\omega t-\varphi_1)}{4} + \frac{i_{a2}\sin(\omega t+\theta-\varphi_2)}{4} \end{aligned} \tag{A5}$$

$$\begin{aligned} i_{c\_Ma\_2\omega} = &\frac{k_1 i_{a1}M_1\cos(2\omega t-\varphi_1)}{8k_2} \\ &- \frac{k_3 i_{a1}M_2\cos(2\omega t+\theta-\varphi_1)}{8k_2} \\ &- \frac{k_1 i_{a2}M_1\cos(2\omega t+\theta-\varphi_2)}{8k_2} \\ &+ \frac{k_3 i_{a2}M_2\cos(2\omega t+2\theta+\varphi_2)}{8k_2} \end{aligned} \tag{A6}$$

$$i_{c\_La\_\mathrm{dc}} = \frac{I_{\mathrm{dc}}}{6} - \frac{i_{a1}M_2\cos(\theta+\varphi_1)}{8} - \frac{i_{a2}M_2\cos(\varphi_2)}{8} \tag{A7}$$

$$\begin{aligned} i_{c\_La\_1\omega} = &\frac{I_{\mathrm{dc}}M_2\sin(\omega t+\theta)}{6} - \frac{i_{a1}\sin(\omega t-\varphi_1)}{4} \\ &- \frac{i_{a2}\sin(\omega t+\theta-\varphi_2)}{4} \end{aligned} \tag{A8}$$

$$\begin{aligned} i_{c\_La\_2\omega} = &\frac{i_{a1}M_2\cos(2\omega t+\theta-\varphi_1)}{8} \\ &+ \frac{i_{a2}M_2\cos(2\omega t+2\theta-\varphi_2)}{8}. \end{aligned} \tag{A9}$$

APPENDIX B

The detailed expressions of $u_{c\_Ua\_1\omega}$, $u_{c\_Ua\_2\omega}$, $u_{c\_Ma\_1\omega}$, $u_{c\_Ma\_2\omega}$, $u_{c\_La\_1\omega}$, and $u_{c\_La\_2\omega}$ are shown as follows:

$$\begin{aligned} u_{c\_Ua\_1\omega} = &\frac{1}{6\omega C}I_{\mathrm{dc}}M_1\cos(\omega t) - \frac{1}{4\omega C}i_{a1}\cos(\omega t-\varphi_1) \\ &- \frac{1}{4\omega C}i_{a2}\cos(\omega t+\theta-\varphi_2) \end{aligned} \tag{B1}$$

$$u_{c\_Ua\_2\omega} = \frac{i_{a1}M_1\sin(2\omega t-\varphi_1)}{16\omega C} + \frac{i_{a2}M_1\sin(2\omega t+\theta-\varphi_2)}{16\omega C} \tag{B2}$$

$$\begin{aligned} u_{c\_Ma\_1\omega} = &-\frac{k_1 I_{\mathrm{dc}}M_1\cos(\omega t)}{6\omega C k_2} + \frac{k_3 I_{\mathrm{dc}}M_2\cos(\omega t+\theta)}{6\omega C k_2} \\ &+ \frac{i_{a1}\cos(\omega t-\varphi_1)}{4\omega C} - \frac{i_{a2}\cos(\omega t+\theta-\varphi_2)}{4\omega C} \end{aligned} \tag{B3}$$

$$\begin{aligned} u_{c\_Ma\_2\omega} = &\frac{k_1 i_{a1}M_1\sin(2\omega t-\varphi_1)}{16\omega C k_2} \\ &- \frac{k_3 i_{a1}M_2\sin(2\omega t+\theta-\varphi_1)}{16\omega C k_2} \\ &- \frac{k_1 i_{a2}M_1\sin(2\omega t+\theta-\varphi_2)}{16\omega C k_2} \\ &+ \frac{k_3 i_{a2}M_2\sin(2\omega t+2\theta-\varphi_2)}{16\omega C k_2} \end{aligned} \tag{B4}$$

$$\begin{aligned} u_{c\_La\_1\omega} = &-\frac{I_{\mathrm{dc}}M_2\cos(\omega t+\theta)}{6\omega C} + \frac{i_{a1}\cos(\omega t-\varphi_1)}{4\omega C} \\ &+ \frac{1}{4\omega C}i_{a2}\cos(\omega t+\theta-\varphi_2) \end{aligned} \tag{B5}$$

$$\begin{aligned} u_{c\_La\_2\omega} = &\frac{i_{a1}M_2\sin(2\omega t+\theta-\varphi_1)}{16\omega C} \\ &+ \frac{i_{a2}M_2\sin(2\omega t+2\theta-\varphi_2)}{16\omega C}. \end{aligned} \tag{B6}$$

APPENDIX C

The detailed expressions of $u_{leg\_1\omega}$, $u_{leg\_2\omega}$, and $u_{leg\_3\omega}$ are shown as follows:

$$\begin{aligned} &u_{leg\_1\omega} \\ &= \frac{\left[8(k_3+k_2-k_1) - k_1 M_1^2 + k_3 M_2^2\right] i_{a1}\cos(\omega t-\varphi_1)}{64\omega C} \end{aligned}$$

$$\begin{aligned}
&+\frac{(k_1^2M_1^2+k_3^2M_2^2)i_{a1}\cos(\omega t-\varphi_1)}{64\omega Ck_2}\\
&+\frac{k_1k_3M_1M_2i_{a2}\cos(\omega t-\varphi_2)}{64\omega Ck_2}\\
&-\frac{\left[\cos(\omega t+\theta-\varphi_1)+\cos(\omega t-\theta-\varphi_1)\right]i_{a1}k_1k_3M_1M_2}{64\omega Ck_2}\\
&+\frac{\left[8(k_3-k_2-k_1)-k_1M_1^2+k_3M_2^2\right]i_{a2}\cos(\omega t+\theta-\varphi_2)}{64\omega C}\\
&-\frac{(k_1^2M_1^2+k_3^2M_2^2)i_{a2}\cos(\omega t+\theta-\varphi_2)}{64\omega Ck_2}\\
&+\frac{i_{a2}k_1k_3M_1M_2\cos(\omega t+2\theta-\varphi_2)}{64\omega C}.
\end{aligned}\tag{C1}$$

$$\begin{aligned}
u_{\mathrm{leg\_}2\omega}=&-\frac{(k_1+k_2)I_{\mathrm{dc}}k_1M_1^2\sin(2\omega t)}{12\omega Ck_2}\\
&+\frac{3i_{a1}k_1M_1\sin(2\omega t-\varphi_1)}{16\omega C}\\
&+\frac{I_{\mathrm{dc}}k_1k_3M_1M_2\sin(2\omega t+\theta)}{12\omega Ck_2}\\
&-\frac{(k_2+k_3)I_{\mathrm{dc}}k_3M_2^2\sin(2\omega t+2\theta)}{24\omega Ck_2}\\
&+\frac{3i_{a2}k_3M_2\sin(2\omega t+2\theta-\varphi_2)}{16\omega C}.
\end{aligned}\tag{C2}$$

$$\begin{aligned}
u_{\mathrm{leg\_}3\omega}=&\frac{(k_2-k_1)k_1i_{a1}M_1^2\cos(3\omega t-\varphi_1)}{64\omega Ck_2}\\
&+\frac{i_{a1}k_1k_3M_1M_2\cos(3\omega t+\theta-\varphi_1)}{32\omega Ck_2}\\
&+\frac{(k_1+k_2)i_{a2}k_1M_1^2\cos(3\omega t+\theta-\varphi_2)}{64\omega Ck_2}\\
&-\frac{(k_2+k_3)i_{a1}k_3M_2^2\cos(3\omega t+2\theta-\varphi_1)}{64\omega Ck_2}\\
&-\frac{i_{a2}k_1k_3M_1M_2\cos(3\omega t+2\theta-\varphi_2)}{32\omega Ck_2}\\
&+\frac{(k_2+k_3)i_{a2}k_3M_2^2\cos(3\omega t+3\theta-\varphi_1)}{64\omega Ck_2}.
\end{aligned}\tag{C3}$$

APPENDIX D

The detailed expressions of capacitor voltage fluctuations in upper, middle, and lower arm under different frequency operation mode of 9A-MMC are shown as follows:

$$\begin{aligned}
u_{c\_Ua}=&\frac{I_{\mathrm{dc}}M_1\cos(\omega_1t)}{6\omega_1C}-\frac{i_{a1}\cos(\omega_1t-\varphi_1)}{4\omega_1C}\\
&-\frac{i_{a2}\cos(\omega_2t+\theta-\varphi_2)}{4\omega_2C}+\frac{i_{a1}M_1\sin(2\omega_1t-\varphi_1)}{16\omega_1C}\\
&+\frac{i_{a2}M_1\sin(\omega_2t-\omega_1t+\theta-\varphi_2)}{8(\omega_1-\omega_2)C}\\
&+\frac{i_{a2}M_1\sin(\omega_2t+\omega_1t+\theta-\varphi_2)}{8(\omega_1+\omega_2)C}
\end{aligned}\tag{D1}$$

$$\begin{aligned}
u_{c\_Ma}=&\frac{i_{a1}\cos(\omega_1\mathrm{t}-\varphi_1)}{4\omega_1C}-\frac{i_{a2}\cos(\omega_2t+\theta-\varphi_2)}{4\omega_2C}\\
&-\frac{k_1I_{\mathrm{dc}}M_1\cos(\omega_1t)}{6\omega_1Ck_2}+\frac{k_3I_{\mathrm{dc}}M_2\cos(\omega_2t+\theta)}{6\omega_2Ck_2}\\
&+\frac{k_1i_{a1}M_1\sin(2\omega_1t-\varphi_1)}{16\omega_1Ck_2}\\
&+\frac{k_3i_{a2}M_2\sin(2\omega_2t+2\theta-\varphi_2)}{16\omega_2Ck_2}\\
&-\frac{k_1i_{a2}M_1\sin(\omega_2t-\omega_1t+\theta-\varphi_2)}{8(\omega_1-\omega_2)Ck_2}\\
&-\frac{k_1i_{a2}M_1\sin(\omega_2t+\omega_1t+\theta-\varphi_2)}{8(\omega_1+\omega_2)Ck_2}\\
&-\frac{k_3i_{a1}M_2\sin(\omega_2t-\omega_1t+\theta-\varphi_1)}{8(\omega_1-\omega_2)Ck_2}\\
&-\frac{k_3i_{a1}M_2\sin(\omega_2t+\omega_1t+\theta-\varphi_1)}{8(\omega_1+\omega_2)Ck_2}
\end{aligned}\tag{D2}$$

$$\begin{aligned}
u_{c\_La}=&-\frac{I_{\mathrm{dc}}M_2\cos(\omega_2t+\theta)}{6\omega_2C}+\frac{i_{a2}\cos(\omega_2t+\theta-\varphi_2)}{4\omega_2C}\\
&+\frac{i_{a1}\cos(\omega_1t-\varphi_1)}{4\omega_1C}+\frac{i_{a2}M_2\sin(2\omega_2t+2\theta-\varphi_2)}{16\omega_2C}\\
&+\frac{i_{a1}M_2\sin(\omega_2t-\omega_1t+\theta-\varphi_1)}{8(\omega_1-\omega_2)C}\\
&+\frac{i_{a1}M_2\sin(\omega_2t+\omega_1t+\theta-\varphi_1)}{8(\omega_1+\omega_2)C}.
\end{aligned}\tag{D3}$$

APPENDIX E

The detailed expression of voltage ripples of one phase leg under different frequency operation mode of 9A-MMC is shown as follows:

$$\begin{aligned}
u_{\mathrm{unba}}(t)=&\frac{\left[8(k_3+k_2-k_1)-k_1M_1^2\right]i_{\mathrm{a1}}\cos(\omega_1t-\varphi_1)}{64\omega_1C}\\
&+\frac{k_1^2M_1^2i_{\mathrm{a1}}\cos(\omega_1t-\varphi_1)}{64\omega_1Ck_2}\\
&+\frac{(k_2+k_3)k_3M_2^2i_{\mathrm{a1}}\cos(\omega_1t-\varphi_1)}{32(\omega_1+\omega_2)Ck_2}\\
&+\frac{(k_2+k_3)k_3M_2^2i_{\mathrm{a1}}\cos(\omega_1t-\varphi_1)}{32(\omega_1-\omega_2)Ck_2}\\
&+\frac{k_1k_3M_1M_2i_{\mathrm{a2}}\cos(\omega_1t+\varphi_2)}{32(\omega_1-\omega_2)Ck_2}\\
&+\frac{k_1k_3M_1M_2i_{\mathrm{a2}}\cos(\omega_1t-\varphi_2)}{32(\omega_1+\omega_2)Ck_2}\\
&-\frac{\left[8(k_1+k_2-k_3)-k_3M_2^2\right]i_{\mathrm{a2}}\cos(\omega_2t+\theta-\varphi_2)}{64\omega_2C}\\
&-\frac{k_3^2M_2^2i_{\mathrm{a2}}\cos(\omega_2t+\theta-\varphi_2)}{64\omega_2Ck_2}
\end{aligned}$$

$$
\begin{aligned}
&- \frac{(k_2+k_1)k_1M_1^2 i_{\mathrm{a2}}\cos(\omega_2 t+\theta-\varphi_2)}{32(\omega_1+\omega_2)Ck_2}\\
&+ \frac{(k_2+k_1)k_1M_1^2 i_{\mathrm{a2}}\cos(\omega_2 t+\theta-\varphi_2)}{32(\omega_1-\omega_2)Ck_2}\\
&+ \frac{k_1k_3M_1M_2 i_{\mathrm{a1}}\cos(\omega_2 t+\theta+\varphi_1)}{32(\omega_1-\omega_2)Ck_2}\\
&- \frac{k_1k_3M_1M_2 i_{\mathrm{a1}}\cos(\omega_2 t+\theta-\varphi_1)}{32(\omega_1+\omega_2)Ck_2}\\
&- \frac{(k_1+k_2)I_{\mathrm{dc}}k_1M_1^2\sin(2\omega_1 t)}{12\omega_1Ck_2}\\
&- \frac{(k_2+k_3)I_{\mathrm{dc}}k_3M_2^2\sin(2\omega_2 t+2\theta)}{24\omega_2Ck_2}\\
&+ \frac{3i_{\mathrm{a1}}k_1M_1\sin(2\omega_1 t-\varphi_1)}{16\omega_1C} + \frac{3i_{\mathrm{a2}}k_3M_2\sin(2\omega_2 t+2\theta-\varphi_2)}{16\omega_2C}\\
&+ \frac{(k_2-k_1)k_1 i_{\mathrm{a1}}M_1^2\cos(3\omega_1 t-\varphi_1)}{64\omega_1Ck_2}\\
&+ \frac{(k_3-k_2)i_{\mathrm{a2}}k_3M_2^2\cos(3\omega_2 t+3\theta-\varphi_2)}{64\omega_2Ck_2}\\
&+ \frac{k_1k_3M_1M_2I_{\mathrm{dc}}\sin(\omega_1 t+\omega_2 t+\theta)}{24\omega_1Ck_2}\\
&+ \frac{k_1k_3M_1M_2I_{\mathrm{dc}}\sin(\omega_1 t+\omega_2 t+\theta)}{24\omega_2Ck_2}\\
&+ \frac{k_1k_3M_1M_2I_{\mathrm{dc}}\sin(-\omega_1 t+\omega_2 t+\theta)}{24\omega_1Ck_2}\\
&- \frac{k_1k_3M_1M_2I_{\mathrm{dc}}\sin(-\omega_1 t+\omega_2 t+\theta)}{24\omega_2Ck_2}\\
&+ \frac{k_1k_3M_1M_2 i_{\mathrm{a1}}\cos(2\omega_1 t+\omega_2 t+\theta-\varphi_1)}{64\omega_1Ck_2}\\
&- \frac{k_1k_3M_1M_2 i_{\mathrm{a1}}\cos(-2\omega_1 t+\omega_2 t+\theta+\varphi_1)}{64\omega_1Ck_2}\\
&- \frac{(k_2+k_1)k_1M_1^2 i_{\mathrm{a2}}\cos(-2\omega_1 t+\omega_2 t+\theta-\varphi_2)}{32(\omega_1-\omega_2)Ck_2}\\
&+ \frac{(k_2+k_1)k_1M_1^2 i_{\mathrm{a2}}\cos(2\omega_1 t+\omega_2 t+\theta-\varphi_2)}{32(\omega_1+\omega_2)Ck_2}\\
&- \frac{k_1k_3M_1M_2 i_{\mathrm{a1}}\cos(-2\omega_1 t+\omega_2 t+\theta+\varphi_1)}{32(\omega_1-\omega_2)Ck_2}\\
&+ \frac{k_1k_3M_1M_2 i_{\mathrm{a1}}\cos(2\omega_1 t+\omega_2 t+\theta-\varphi_1)}{32(\omega_1+\omega_2)Ck_2}\\
&- \frac{k_1k_3M_1M_2 i_{\mathrm{a2}}\cos(\omega_1 t+2\omega_2 t+2\theta-\varphi_2)}{64\omega_2Ck_2}\\
&+ \frac{k_1k_3M_1M_2 i_{\mathrm{a2}}\cos(-\omega_1 t+2\omega_2 t+2\theta-\varphi_2)}{64\omega_2Ck_2}\\
&- \frac{(k_2+k_3)k_3M_2^2 i_{\mathrm{a1}}\cos(-\omega_1 t+2\omega_2 t+2\theta+\varphi_1)}{32(\omega_1-\omega_2)Ck_2}\\
&- \frac{(k_2+k_3)k_3M_2^2 i_{\mathrm{a1}}\cos(\omega_1 t+2\omega_2 t+2\theta-\varphi_1)}{32(\omega_1+\omega_2)Ck_2}\\
&- \frac{k_1k_3M_1M_2 i_{\mathrm{a2}}\cos(-\omega_1 t+2\omega_2 t+2\theta-\varphi_2)}{32(\omega_1-\omega_2)Ck_2}\\
&- \frac{k_1k_3M_1M_2 i_{\mathrm{a2}}\cos(\omega_1 t+2\omega_2 t+2\theta-\varphi_2)}{32(\omega_1+\omega_2)Ck_2}.
\end{aligned}
$$

REFERENCES

[1] M. Saeedifard and R. Iravani, “Dynamic performance of a modular multilevel back-to-back HVDC system,” *IEEE Trans. Power Del.*, vol. 25, no. 4, pp. 2903–2912, Oct. 2010.

[2] A. Nami, J. Liang, F. Dijkhuizen, and G. D. Demetriades, “Modular multilevel converters for HVDC applications: Review on converter cells and functionalities,” *IEEE Trans. Power Electron.*, vol. 30, no. 1, pp. 18–36, Jan. 2015.

[3] M. Guan and Z. Xu, “Modeling and control of a modular multilevel converter-based HVDC system under unbalanced grid conditions,” *IEEE Trans. Power Electron.*, vol. 27, no. 12, pp. 4858–4867, Dec. 2012.

[4] X. Liu, J. Lv, C. Gao, Z. Chen, and S. Chen, “A novel STATCOM based on diode-clamped modular multilevel converters,” *IEEE Trans. Power Electron.*, vol. 32, no. 8, pp. 5964–5977, Aug. 2017.

[5] H. P. Mohammadi and M. T. H. Bina, “A transformerless medium-voltage STATCOM topology based on extended modular multilevel converters,” *IEEE Trans. Power Electron.*, vol. 26, no. 5, pp. 1534–1545, May 2011.

[6] Q. Hao, J. Man, F. Gao, and M. Guan, “Voltage limit control of modular multilevel converter based unified power flow controller under unbalanced grid conditions,” *IEEE Trans. Power Del.*, vol. 33, no. 3, pp. 1319–1327, Jun. 2018.

[7] B. Tai, C. Gao, X. Liu, and Z. Chen, “A novel flexible capacitor voltage control strategy for variable-speed drives with modular multilevel converters,” *IEEE Trans. Power Electron.*, vol. 32, no. 1, pp. 128–141, Jan. 2017.

[8] B. Li, S. Zhou, D. Xu, S. J. Finney, and B. W. Williams, “A hybrid modular multilevel converter for medium-voltage variable-speed motor drives,” *IEEE Trans. Power Electron.*, vol. 32, no. 6, pp. 4619–4630, Jun. 2017.

[9] R. Marquardt and A. Lesnicar, “A new modular voltage source inverter topology,” in *Proc. Eur. Power Electron. Conf.*, 2003, pp. 1–10.

[10] A. Lesnicar and R. Marquardt, “An innovative modular multilevel converter topology suitable for a wide power range,” in *Proc. IEEE Power Tech. Conf.*, 2003, vol. 3, pp. 1–6.

[11] M. S. Diab, A. M. Massoud, S. Ahmed, and B. W. Williams, “A dual modular multilevel converter with high-frequency magnetic links between submodules for MV open-end stator winding machine drives,” *IEEE Trans. Power Electron.*, vol. 33, no. 6, pp. 5142–5159, Jun. 2018.

[12] J. Fu, B. Zhang, and D. Qiu, “A novel nine-arm modular multilevel converter,” in *Proc. 40th Annu. Conf. IEEE Ind. Electron. Soc.*, 2014, pp. 4528–4533.

[13] A. A. Elserougi, A. S. Abdel-Khalik, A. M. Massoud, and S. Ahmed, “A nine-arm modular multilevel converter (9A-MMC) for six-phase medium voltage motor drives,” in *Proc. 4th Int. Conf. Elect. Power Energy Convers. Syst.*, 2015, pp. 1735–1740.

[14] A. A. Elserougi, A. S. Abdel-Khalik, A. M. Massoud, and S. Ahmed, “An asymmetrical six-phase induction motor drive based on nine-arm modular multilevel converter (9AMMC) with circulating current suppression,” in *Proc. IEEE-EPECS*, 2015, pp. 1–6.

[15] M. S. Diab, G. P. Adam, B. W. Williams, A. M. Massoud, and S. Ahmed, “Quasi two-level PWM operation of a nine-arm modular multilevel converter for six-phase medium-voltage motor drives,” in *Proc. IEEE Appl. Power Electron. Conf. Expo.*, 2018, pp. 1641–1648.

[16] T. Kominami and Y. Fujimoto, “A novel nine-switch inverter for independent control of two three-phase loads,” in *Proc. IEEE Ind. Appl. Annu. Meeting*, 2007, pp. 2346–2350.

[17] F. Gao, L. Zhang, D. Li, P. C. Loh, Y. Tang, and H. Gao, “Optimal pulsewidth modulation of nine-switch converter,” *IEEE Trans. Power Electron.*, vol. 25, no. 9, pp. 2331–2343, Sep. 2010.

[18] Y. Zhou, J. Jiang, J. Guo, P. Hu, and Y. Liang, “Analysis and control of modular multilevel converters under unbalanced conditions,” *IEEE Trans. Power Del.*, vol. 28, no. 4, pp. 1986–1995, Oct. 2013.

[19] M. A. Perez, S. Bernet, J. Rodriguez, S. Kouro, and R. Lizana, “Circuit topologies, modelling, control schemes and applications of modular multilevel converters,” *IEEE Trans. Power Electron.*, vol. 30, no. 1, pp. 4–17, Mar. 2014.

[20] J. Wang, J. Liang, F. Gao, X. Dong, C. Wang, and B. Zhao, “A closed-loop time-domain analysis method for modular multilevel converter,” *IEEE Trans. Power Electron.*, vol. 32, no. 10, pp. 7494–7508, Oct. 2017.

[21] Q. Song, W. Liu, X. Li, H. Rao, S. Xu, and L. Li, “A steady-state analysis method for a modular multilevel converter,” *IEEE Trans. Power Electron.*, vol. 28, no. 8, pp. 3702–3713, Aug. 2013.

[22] A. Dekka, B. Wu, R. L. Fuentes, M. Perez, and N. R. Zargari, “Evolution of topologies, modeling, control schemes, and applications of modular multilevel converters,” *IEEE J. Emerg. Sel. Topics Power Electron.*, vol. 5, no. 4, pp. 1631–1656, Dec. 2017.

[23] S. Debnath, J. Qin, B. Bahrani, M. Saeedifard, and P. Barbosa, “Operation, control, and applications of the modular multilevel converter: A review,” *IEEE Trans. Power Electron.*, vol. 30, no. 1, pp. 37–53, Jan. 2015.

[24] M. Hagiwara and H. Akagi, “Control and experiment of pulsewidth modulated modular multilevel converters,” *IEEE Trans. Power Electron.*, vol. 24, no. 7, pp. 1737–1746, Jul. 2009.

[25] B. Bahrani, S. Debnath, and M. Saeedifard, “Circulating current suppression of the modular multilevel converter in a double-frequency rotating reference frame,” *IEEE Trans. Power Electron.*, vol. 31, no. 1, pp. 783–792, Jan. 2016.

[26] Q. Tu, Z. Xu, and L. Xu, “Reduced switching-frequency modulation and circulating current suppression for modular multilevel converters,” *IEEE Trans. Power Del.*, vol. 26, no. 3, pp. 2009–2017, Jul. 2011.

[27] X. Li, Q. Song, W. Liu, S. Xu, Z. Zhu, and X. Li, “Performance analysis and optimization of circulating current control for modular multilevel converter,” *IEEE Trans. Ind. Electron.*, vol. 63, no. 2, pp. 716–727, Feb. 2016.

[28] M. Liserre, R. Teodorescu, and F. Blaabjerg, “Multiple harmonics control for three-phase grid converter systems with the use of PI-RES current controller in a rotating frame,” *IEEE Trans. Power Electron.*, vol. 21, no. 3, pp. 836–840, May 2006.

[29] S. Li, X. Wang, Z. Yao, T. Li, and Z. Peng, “Circulating current suppressing strategy for MMC-HVDC based on nonideal proportional resonant controllers under unbalanced grid conditions,” *IEEE Trans. Power Electron.*, vol. 30, no. 1, pp. 387–397, Jan. 2015.

Futian Qin (S’18) received the B.Eng. degree in electrical engineering from Shandong Agricultural University, Tai’an, China, in 2015. He is currently working toward the Ph.D. degree in electrical engineering with Shandong University, Jinan, China.

His research interests include modular multilevel converters, HVdc, and FACTS.

Feng Gao (S’07–M’09–SM’18) received the B.Eng. and M.Eng. degrees in electrical engineering from Shandong University, Jinan, China, in 2002 and 2005, respectively, and the Ph.D. degree from the School of Electrical and Electronic Engineering, Nanyang Technological University, Singapore, in 2009.

From 2008 to 2009, he was a Research Fellow with Nanyang Technological University. In 2010, he joined the School of Electrical Engineering, Shandong University, where he is currently a Professor. From September 2006 to February 2007, he was a Visiting Scholar with the Institute of Energy Technology, Aalborg University, Aalborg, Denmark.

Dr. Gao was the recipient of the IEEE Industry Applications Society Industrial Power Converter Committee Prize for a paper published in 2006 and 2017 IEEE Power Electronics Transactions Second Prize Paper Award, and he is currently serving as the Associate Editor of IEEE TRANSACTIONS ON POWER ELECTRONICS and *CPSS Transcations on Power Electronics and Applications*.

Chenghui Zhang (M’14–SM’18) was born in Shandong, China, in 1963. He received the B.S. and M.S. degrees in automation engineering from the Shandong University of Technology, Jinan, China, in 1985 and 1988, respectively, and the Ph.D. degree in control theory and operational research from Shandong University, Jinan, in 2001.

In 1988, he joined Shandong University, where he is currently a Full Professor with the School of Control Science and Engineering, and the Director of the Research Center of Power Electronics Energy-Saving Technology and Equipment, Chinese Education Ministry. He was selected as a Changjiang Scholar of the Education Ministry in 2009 and a Taishan Scholar of Shandong Province in 2009. His current research interests include optimal control of engineering, power electronics and motor drives, and energy-saving techniques.